Title:

Tracking infectious entry routes of SARS-CoV-2

Authors:

Alex J.B. Kreutzberger [a,b], Anwesha Sanyal [a,b], Anand Saminathan [a,b], Louis-Marie Bloyet [c], Spencer Stumpf [c], Zhuoming Liu [c], Ravi Ojha [d], Markku T. Patjas [e], Ahmed Geneid [e], Gustavo Scanavachi [a,b], Catherine A. Doyle [f], Elliott Somerville [b], Ricardo Bango Da Cunha Correira [a,b], Giuseppe Di Caprio [b,g], Sanna Toppila-Salmi [h], Antti Mäkitie [e], Volker Kiessling [i], Olli Vapalahti [d,j,k], , Sean P.J. Whelan [c,*], Giuseppe Balistreri [d,j,l *], and Tom Kirchhausen [a,b,g,*]

Affiliations:

[a] Department of Cell Biology, Harvard Medical School, 200 Longwood Av, Boston, MA 02115, USA

[b] Program in Cellular and Molecular Medicine, Boston Children's Hospital, 200 Longwood Av, Boston, MA 02115, USA

[c] Department of Molecular Microbiology, Washington University in Saint Louis, 660 South Euclid Avenue, Saint Louis, MI 63110, USA

[d] Department of Virology, Faculty of Medicine, University of Helsinki, Helsinki, Finland

[e] Department of Otorhinolaryngology and Phoniatrics, Head and Neck Surgery, University of Helsinki and Helsinki University Hospital, Helsinki, Finland.

[f] Department of Pharmacology, University of Virginia, Charlottesville, VA 22903

[g] Department of Pediatrics, Harvard Medical School, 200 Longwood Ave, Boston, MA 02115, USA

[h] Department of Allergy, University of Helsinki and Helsinki University Hospital, Helsinki, Finland.

[i] Center for Membrane and Cell Physiology and Department of Molecular Physiology and Biological Physics, University of Virginia, Charlottesville, VA 22903

[j] Department of Veterinary Biosciences, University of Helsinki, Helsinki, Finland

[k] Virology and Immunology, Helsinki University Hospital Diagnostic Center (HUSLAB), Helsinki, Finland

[l] The Queensland Brain Institute, University of Queensland, Brisbane, Australia

[*] Corresponding authors.

kirchhausen@crystal.harvard.edu (T.K.)

giuseppe.balistreri.fi (G.B.)
spjwhelan@wustl.edu (S.P.J.W.)

One sentence summary:

Detailed molecular snapshots of the productive infectious entry pathway of SARS-CoV-2 into cells

ABSTRACT:

SARS-CoV-2 cell entry starts with membrane attachment and ends with spike-protein (S) catalyzed membrane fusion depending on two cleavage steps, one usually by furin in producing cells and the second by TMPRSS2 on target cells. Endosomal cathepsins can carry out both. Using real-time 3D single virion tracking, we show fusion and genome penetration requires virion exposure to an acidic milieu of pH 6.2-6.8, even when furin and TMPRSS2 cleavages have occurred. We detect the sequential steps of S1-fragment dissociation, fusion, and content release from the cell surface in TMPRRS2 overexpressing cells only when exposed to acidic pH. We define a key role of an acidic environment for successful infection, found in endosomal compartments and at the surface of TMPRSS2 expressing cells in the acidic milieu of the nasal cavity.

Significance Statement:

Infection by SARS-CoV-2 depends upon the S large spike protein decorating the virions and is responsible for receptor engagement and subsequent fusion of viral and cellular membranes allowing release of virion contents into the cell. Using new single particle imaging tools, to visualize and track the successive steps from virion attachment to fusion, combined with chemical and genetic perturbations of the cells, we provide the first direct evidence for the cellular uptake routes of productive infection in multiple cell types and their dependence on proteolysis of S by cell surface or endosomal proteases. We show that fusion and content release always require the acidic environment from endosomes, preceded by liberation of the S1 fragment which depends on ACE2 receptor engagement.

61 **Main Text:**

62 SARS-CoV-2 cell entry begins with engagement at the cell-surface and ends with deposition of
63 the viral contents into the cytosol by membrane fusion. The first step is binding of the viral spike
64 protein (S) with its cellular receptor, angiotensin converting enzyme (ACE2) (*1–4*). The last step
65 delivers the viral genomic RNA in association with the nucleocapsid protein (N), which is removed
66 for translation of the input genome (*5*, *6*). Proteolytic activation of S by additional host-cell factors
67 is necessary for it to function as a fusogen. Cleavage of S by furin in producer cells (*7*) generates
68 the S1 receptor binding subunit non-covalently associated with the S2 fusion subunit. The S
69 protein is cleaved by cell surface or endosomal proteases during virion entry into host cells, that
70 activate the viral fusion machinery (*1*, *8–10*). This entry associated proteolysis of S has led to the
71 current model of two routes of infectious cell entry: fusion of viral and cellular membranes at the
72 host-cell surface or fusion following endosomal uptake (*6*).
73
74 The cellular proteases that are involved in processing S during entry include the transmembrane
75 serine proteases TMPRSS2 or TMPRSS4 found at the cell surface (*1*, *8*), and the endosomal
76 cathepsins that require the acidic milieu of the compartments in which they are enriched (*1*, *10*).
77 Processing of S by TMPRSS proteases or by cathepsins, at a site designated S2', depends on
78 prior cleavage at the furin site in the producer cells (*7*, *11*, *12*). TMPRSS cleavage has been
79 thought to result in infection from the plasma membrane and cathepsin cleavage, in cells lacking
80 TMPRSS activity, with infection from endosomes (*5*, *6*). Chemical inhibitors of TMPRSS or
81 cathepsin proteases in cells in culture indeed show that infection of some cell types is more
82 sensitive to inhibition of endosomal cathepsins whereas others are more sensitive to inhibition of
83 TMPRSS proteases (*1*, *9*). TMPRSS inhibitors such as camostat and nafamostat are in clinical
84 development as SARS-CoV-2 therapeutics, further highlighting the need to understand how entry
85 pathways depend upon specific proteases.
86
87 To analyze the routes of cellular uptake that lead to successful fusion and release of virion
88 contents into the cytoplasm, we developed a set of new tools that allow direct visual tracking of
89 the uptake of single virions and release of their contents. Using a chimeric vesicular stomatitis
90 virus (VSV) in which SARS-CoV-2 S has replaced the endogenous glycoprotein gene (G), we
91 modified the virus to permit the separate tracking of the S protein and the viral contents. We
92 engineered a structural component of the replicative core of VSV, the phosphoprotein (P), to
93 append to its amino terminus enhanced green fluorescent protein (eGFP), for tracking the virion
94 content. This eGFP-P chimeric virus is structurally fluorescent and depends upon S for entry. We

also sparsely labelled the S protein by direct conjugation with a fluorescent dye, allowing us to visualize the steps of entry, from S1 fragment release to membrane fusion, including virion content release into cells during productive infection. We have found that content release requires acidic pH and that it occurs principally from endosomes irrespective of the cell type and irrespective of the dependence of the virus on TMPRSS2 or cathepsin-mediated processing of S. Only mild acidification of the medium allows efficient entry at the plasma membrane. We correlate our findings with studies of infection by several human isolates of SARS-CoV-2.

RESULTS

Cell entry of individual virions mediated by SARS-CoV-2 S

We used live-cell fluorescence microscopy to monitor uptake of single VSV-SARS-CoV-2 virions that depend upon SARS-CoV-2 S for infection (Wuhan Hu-1 isolate and Delta and Omicron variants, chimeras generated as described: see Methods and (*13*)) and for the Wuhan variant also containing a fluorescent internal structural protein, P, fused at its amino terminus to eGFP (eGFP-P) (Fig. S1). We counted the number of tagged particles internalized 1 hr post inoculation at MOI 0.5 and found 50-70 particles in Caco-2, Calu-3, and Vero cells, but about three times that number in Vero-TMPRSS2 cells, which overexpress TMPRSS2 (Fig. S1D, E), presumably because of more efficient TMPRSS2 cleavage in the high expression cell line. Examination of the labeled virions by spinning-disc confocal microscopy showed distinct, diffraction-limited puncta with a single, Gaussian distribution of fluorescent intensities (Fig. S2A), consistent with the presence of single virus particles and absence of virion aggregates. We also labeled the S protein sparsely with the fluorescent dye Atto565 NHS ester (25-35 dyes per virion), with minimal effect on particle infectivity (Fig. S2A-D). The double labeling allowed us to track the viral S protein separately from the virion contents.

SARS-CoV-2 S-mediated entry requires endocytic uptake

We used live-cell volumetric, lattice-light-sheet fluorescence microscopy (LLSM) (*14*) to obtain 3D views of virion cell-entry over time during their uptake into cells (Figs. 1A-E, Fig S3). We incubated cells for 8 min, transferred them to the LLSM, and recorded sequential 3-D stacks from a single cell, acquiring a full stack every 2 sec, for 10 min (300 stacks total). We then moved quickly to an adjacent cell and recorded a similar 10 min series of 300 stacks, after which we moved finally to a third neighboring cell, for 10 min. The sequence of representative 10-plane projections in Fig. 1B shows that particles attached to the cell surface during the initial 8 min incubation, followed by efficient internalization at later time points. The figure shows images from Vero-TMPRSS2

129 cells; we obtained similar results for Vero, Caco-2 and Calu-3 cells, as shown in Fig S3. The views
130 from 20- and 30-minutes post-inoculation also showed many examples of intracellular spots
131 labeled with eGFP-P only, representing delivery of the VSV ribonucleoprotein core (RNP) into
132 cells visualized as the separation of fluorescent eGFP-P from the membrane-bound, Atto565
133 labelled S glycoprotein.
134
135 We confirmed that the views in Fig 1B reflected the outcome of sequential internalization and
136 RNP delivery events by tracking individual particles in the volumetric time series acquired using
137 LLSM (Fig. 1C). Single virions attached to cells during the 8 min period following addition of virus,
138 and ~ 90% (1508/1692) of the attached particles had internalized during the 30 min time course,
139 as recorded in 60 time-lapse 3D videos from 20 cells. The representative 10-plane projection in
140 Fig. 1C obtained during the initial 10-minute interval shows several single-particle examples of
141 virion internalization and three events of RNP core release (for similar results with Vero, Caco-2
142 and Calu-3 cells, see Fig S3). The highlighted example in Fig. 1C and the complete ortho
143 projection in Fig. 1D show a fluorescent spot corresponding to a virus particle, first captured at
144 the cell surface, then undergoing rapid directed movement towards the cell interior, due to
145 endocytosis and intracellular traffic of virus-containing vesicles. Dissociation of the eGFP-P from
146 the Atto565 signals marks delivery of the genome into the cytosol (see also Figs. S3-S7). In a
147 total of 60 Caco-2, Calu-3, Vero and Vero-TMPRSS2 cells, we detected separation of signals at
148 an intracellular location for 138/1692 trajectories during the 30-min interval starting two minutes
149 after an initial 8-minute inoculation (Fig. 1E), and only one dissociation event at the cell surface
150 (for a Vero-TMPRSS2 cell). The fluorescent signals from eGFP-P released in these times frames
151 remained stable and punctate in the cytosol during the duration of the 10 min acquisition, and any
152 released eGFP-P in the cytosol at the outset of the second or third 10 min time series remained
153 stable for the entire 10 min recording. Moreover, we never observed uncoated (delivered)
154 particles (i.e., released eGFP-P) in the early frames of the time lapse from the first cell. These
155 observations rule out the possibility of rapid, early entry events from the cell surface or from
156 endosomes during the "blind" 8 minutes during inoculation, and we conclude that an endocytic
157 route accounted for all but one of the detected VSV-SARS-CoV-2 fusion events in these
158 experiments.
159
160 Analysis of mean square displacement (MSD) curves from three-dimensional, single-particle
161 trajectories allowed us to determine the dynamic regime of the particle at any time point after
162 attachment. The alpha coefficient (α) in the anomalous diffusion equation ($\langle r^2 \rangle = 6Dt^{\alpha}$)

163 corresponds to confined motion (α < 0.8) for the virus attached to the cell surface, directed motion
164 (α >1.2) for intracellular particles with co-localized Atto565-labelled S and eGFP-P labelled RNP,
165 presumably associated with endosomes, and Brownian motion (0.8< α <1.2) for eGFP-P spots
166 diffusing in the cytosol. The results shown in Fig. 1F (which corresponds to the viral particle traced
167 in Figs. 1 C and D) and the summary for all tracked particles in Fig. 1G (see also Fig. S3-S7)
168 illustrate the moment at which an RNP escapes into the cytosol (α = 1.07), while the tagged S
169 remains associated with an endosome (α = 1.93, see below).
170
171 The chimeric VSV particles are roughly 80 by 200 nm (*15*, *16*) and appear in the microscope as
172 diffraction-limited spots. Endosomes typically range in diameter from 300-1000 nm (*17*). Thus, a
173 subset of fluorescent endosomes are larger than the diffraction limit, facilitating use of an
174 increased apparent size of an Atto565 fluorescent spot as a proxy for viral membrane fusion with
175 the surrounding (larger) endosomal membrane (Fig. S8). Using this approach, we detected fusion
176 in 17 $\pm$ 4 % (n = 20 virions), 28 $\pm$ 2% (n = 61 virions), 23 $\pm$ 2% (n = 27 virions), and 27 $\pm$ 6% (n =
177 30 virions) of the traces in Vero, Vero-TMPRSS2, Caco-2 or Calu-3 cells, respectively. All the
178 events coincided with release into the cytosol of the eGFP-P labeled RNP core of VSV (Figs. 1E,
179 S3, S7). We did not observe release of the virion contents at the plasma membrane (Figs. 1E,
180 S3-S7), indicating that S-mediated infection of cells only occurred through an endocytic pathway.
181
182 **SARS-CoV-2 S-mediated infection requires endocytosis**
183 Dynamin, a large GTPase required for cargo uptake in clathrin-mediated or fast endophilin-
184 mediated endocytosis (*18*), is susceptible to interference by a dominant negative mutant, K44A
185 (*19*). To test whether dynamin-dependent endocytosis is necessary for SARS-CoV-2 S mediated
186 infection, we transiently over expressed the dominant-negative mutant in Caco-2, Calu-3, Vero
187 and Vero-TMPRSS2 cells. We monitored the effect on infection of these cells by VSV-SARS-
188 CoV-2 that expresses eGFP as a marker of infection (VSV-eGFP-SARS-CoV-2) according to the
189 scheme summarized in Fig S9A, and we quantified infection by single-cell imaging at 8 hours post
190 inoculation. In control cells, to achieve comparable infectivity we used 10 times more VSV-SARS-
191 CoV-2 for Caco-2 and Calu-3 cells than for Vero or Vero-TMPRSS2 over-expressing TPMRSS2
192 (Figs. S9B, C). Irrespective of the cell type, infection was inhibited by the dominant negative
193 dynamin mutant (Fig 1H) or by addition of dynasore-OH, a small molecule dynamin inhibitor (*20*)
194 (Fig. 1I). Dynasore-OH addition at 1h post-inoculation had no effect on viral infectivity, consistent
195 with inhibition of an early, entry-related event, but not with later inhibition of viral gene expression
196 (Fig. S9C). We previously reported that S mediated infection of cells by VSV-SARS-CoV-2

197 correlates well with infection by SARS-CoV-2 (*9*, *13*, *21*, *22*). In accord with that correlation,
198 dynasore-OH also inhibited infection of Calu-3 and Vero-TMPRSS2 cells by a SARS-CoV-2
199 Wuhan (B.1) clinical isolate (Fig 1J). These results show a critical role for endocytosis in SARS-
200 CoV-2 infection of multiple cell types in culture including cells that express TMPRSS2.
201
202 **Viral entry from endosomes**
203 Our data show that internalized virus particles reached internal membrane compartment(s) from
204 which fusion and genome entry into the cytosol occurred. To establish the identity of the(se)
205 endosomal compartments, we used live-cell LLSM to track particles entering SVG-A cells
206 ectopically expressing ACE2, or both ACE2 and TMPRSS2, and gene-edited for fluorescent
207 labeling of specific endosomal compartments. (Fig. 2A, S10). Single particle tracking of 6815
208 viruses over a 50 min period starting from 30 minutes post inoculation of cells revealed VSV-
209 SARS-CoV-2 particles trafficked from the cell surface to early endosomes marked with early
210 endosomal antigen 1 fused to the fluorescent protein Scarlett (EEA1-mScarlett) and subsequently
211 to late endosomes/lysosomes marked with a Halo-tagged version of the cholesterol transporter
212 Niemann Pick C1 NPC1-Halo-JFX646 (examples for single virions shown in Fig 2 B, C, S11-S12).
213 We only detected particles located in the interior localizing with the endosomal markers in early
214 frames of the time lapse from the first cell taken at the end of the 30 min inoculation period. Like
215 with the other cells, these observations also rule out for SVG-A cells the possibility of entry events
216 from the cell surface or from endosomes during the 30-min inoculation period.
217
218 To establish the location of the compartments from which the virion contents were released, we
219 identified the point at which the trajectory of the eGFP-P signal changed from directed (α >1.2) to
220 Brownian (0.8< α <1.2) concomitant with a loss of co-localization with endosomal markers
221 (examples for single virions shown in Fig 2 D, E, S13-S14). All entry events occurred from
222 compartments marked with either EEA1 or NPC1 in cells expressing TMPRSS2, and only from
223 NPC1-compartments in cells lacking TMPRSS2 (Fig. 2 F, S15).
224
225 **Release of S1 at the surface of cells expressing TMPRSS2**
226 Membrane fusion mediated by S depends on its proteolytic cleavage and dissociation of the S1
227 fragment (*6*). Cleavage alone does not release S; the required trigger is ACE2 binding. Addition
228 of soluble ACE2 ectodomain to VSV-SARS-CoV-2 particles activated by trypsin, to bypass
229 TMPRSS2, released about 70% of the Atto 565 label, a reasonable estimate of the fraction of S1
230 rather than S2. In live-cell imaging experiments with TMPRSS2 expressing cells, we noted a

231 partial loss of Atto 565 intensity from labeled VSV-SARS-CoV-2 particles after they attached to
232 the cell surface (Fig. S19). In these experiments, we used a microfluidics device to introduce virus
233 to cells while in the LLSM, enabling us to detect attachment directly. We interpreted the loss of
234 Atto 565 signal as S1 dissociation, and we took it as a proxy for cleavage by TMPRSS2 at the S2'
235 site on an ACE2-attached spike protein. Dissociated S1 will remain attached to ACE2 for some
236 time, and in about ~2 % of the events, we could indeed detect lateral spreading (interpreted as
237 diffusion in the plasma membrane) associated with the abrupt partial reduction of the punctate
238 Atto 565 signal. We found ~25% loss of the Atto 565 signal per particle in ~ 78% of particles at
239 the surface of Vero-TMPRSS2 cells expressing TMPRSS2 (Fig. 3 A-D) within the first 10 min of
240 LLSM single-particle tracking (Fig. 1E). In all cases the loss was in a single step with a half time
241 of 2 sec or less (Fig. 3B and Fig. S16). The signal reduction, which preceded endocytosis, was
242 never associated with RNP delivery (e.g., eGFP-P) from the cell surface (Fig. 1E, cell #1), except
243 under the special circumstances of slightly acidic medium during inoculation as described in the
244 following section (Fig. 3 E-J and Fig. 4). The signal loss at the cell surface depended strictly on
245 TMPRSS2 activity, as it was inhibited by 10 μM Camostat and was absent in Vero cells lacking
246 TMPRSS2 (Fig 3D). The decrease in punctate intensity, which we interpret as release of S1,
247 occurred in less than 5% of particles attached to Caco-2 or Calu-3 cells, which naturally express
248 TMPRSS2 (Fig. 3D). This result suggests that in these cells, cleavage at S2' by TMPRSS2 occurs
249 primarily after uptake into endosomes.
250
251 **Viral membrane fusion requires acidic pH**
252 Endosomes undergo rapid acidification, and acidic pH is a trigger that induces fusogenic
253 conformational changes in many viral envelope proteins. We therefore examined the effect of pH
254 on productive viral entry by adjusting the pH of the medium at 10 minutes post inoculation. From
255 187 traces from VERO-TMPRSS2 cells incubated at pH 6.8, we observed 84 fusion events at the
256 cell surface, as defined by loss of Atto 565 signal and by accompanying eGFP-P delivery into the
257 cytosol (Fig. 3 E-H, S17). The abrupt partial loss of punctate signal, interpreted as S1-fragment
258 release, always preceded fusion (signaled by diffusion in the plasma membrane of the remaining
259 Atto 565 signal with a half-life of about 20 sec) and by eGFP-P delivery into the cytosol, typically
260 within 10 sec (Fig. 3 E, F). We defined eGFP-P delivery into the cytosol by a change in its motion
261 from confined (α <0.8) when on the cell surface to Brownian (0.8< α <1.2) when in the cytosol
262 (Fig. 3G). In the absence of S1-release, we did not detect S1 diffusion or eGFP-P delivery into
263 the cytosol. We conclude that release of S1 and subsequent or concomitant exposure to acidic
264 pH result in release of virion contents into the cell.

Incubation of Vero-TMPRSS2 cells at pH 6.2 rather than 6.8 during inoculation prevented release of the S1-fragment and hence prevented viral fusion at the cell surface (Fig. 3 E, G, and H). This pH dependence is consistent with an expected loss of TMPRSS2 proteolytic activity as the pH falls below 7. When cells were incubated at pH 7.4 throughout infection, we did not observe any particle fusion and content release at the cell surface, even though TMPRSS2 cleavage, as detected by S1-fragment release, still occurred (Fig. 3 E, G and H).

The efficiency of entry by VSV-SARS-CoV-2 tracked by visualizing content release or by extent of infection increased in Vero-TMPRSS2 cells at pH 6.8 (Fig. 3H). To investigate further the requirement of acidic pH for efficient SARS-CoV-2 S-mediated membrane fusion, we carried out bypass experiments to initiate infection directly at the cell surface. We blocked endocytic uptake into cells with dynasore-OH and exposed bound particles to different pH ranging from 6.2-7.4. Infection of Vero, Caco-2 or Calu-3 cells was blocked regardless of the pH, whereas Vero cells overexpressing TMPRSS2 were readily infected by acid triggering of the S protein at the cell surface (Fig. 3J, S18).

These results were consistent with the observed lack of release of the S1-fragment from viruses at the surface of Vero, Caco-2, or Calu-3 cells (Fig. 3D). To eliminate a requirement for TMPRSS2 cleavage of S, we pre-activated particles by incubation with trypsin before inoculating the cells. These pre-activated particles were as infectious in Vero-E6 TM cells treated with dynasore-OH and inoculated at pH < 7 as non-trypsinized particles in the same cells and conditions. Thus, trypsin and TMPRSS2 cleavages were equally effective in activating the particles. With progressive acidification of the medium, infection increased, reaching a maximum at pH 6.6 and remaining constant to pH 6.2 (Fig. 3H). These results show that S-mediated fusion requires pH < 7. We obtained similar results concerning the effect of pH on infectivity of authentic SARS-CoV-2 with cells in which endocytosis was blocked and genome penetration depended solely on cell-surface fusion events (Fig 3I-J).

Influence of S protein variation on infectious entry pathways

We found that response to infection inhibitors and the requirement for endocytosis and proteolytic cleavage of S for the VSV chimera with the Delta variant S protein were essentially the same for the chimera with the S protein from the original Wuhan-Hu1 isolate (Fig. 4A-D and S20, S21). Conserved events included release of the S1-fragment from receptor-bound virions attached to

299 Vero-TMPRSS2 cells (Fig. 4 B), and S1 release followed by fusion and genome penetration when
300 inoculation was at pH 6.5-6.8 (Fig. 4C). Both Wuhan-Hu1 and Delta also showed enhanced
301 infectivity of Vero-TMPRSS2 cells inoculated at pH 6.8 (Fig. E-G).
302
303 Examination of the entry pathway mediated by the S protein of Omicron varied with the cell type
304 used to produce the virus. VSV-Omicron produced in Vero-TMPRSS2 cells depended on
305 TMPRSS2 activation for infection of Vero-TMPRSS2, although somewhat fewer virions released
306 the S1 fragment at the cell surface (Fig 4B-D). VSV-SARS-CoV-2 chimeras with Omicron S
307 produced in MA104 cells could not be activated by TMPRSS2 and failed to infect or fuse from the
308 surface of Vero-TMPRSS2 cells at pH 6.8 (Fig. 4A-D, S20, S21). Infection required activation by
309 cathepsins for fusion and infection from endosomes (Fig 4 A-D, S20, S21). Trypsin treatment of
310 VSV-SARS-CoV-2-Omicron, which cleaves at both the furin and TMPRSS protease sites (*23*),
311 allowed infection to proceed from the cell surface at acidic pH, independent of the producer cell
312 line, even in the presence of an endocytosis inhibitor (Fig.4A-D, S20, S21).
313
314 Sequence analysis of the genomic RNA from the VSV-SARS-CoV-2 chimeric viruses confirmed
315 the presence of the TMPRSS2 and furin cleavage sites in Omicron S. As furin cleavage in
316 producing cells is essential for subsequent proteolysis by TMPRSS2 in the infecting cell, we
317 tested whether incomplete furin cleavage explained the differential susceptibility to TMPRSS2
318 activation. We found much less cleavage of Omicron S for virus produced in MA104 cells (Fig 4D)
319 than for virus produced in Vero-TMPRSS2 cells (Fig. 4D). Particles with furin cleaved S were
320 susceptible to TMPRSS2 activation (Fig 4A-D), released the S1-fragment (Fig 4A), and fused at
321 pH 6.8 (Fig. 4 B,D).
322
323 **Intranasal pH**
324 Our results suggest that an acidic environment is required for successful infection, found in
325 endosomal compartments and at the surface of TMPRSS2 expressing cells purposely exposed
326 to mildly acidic extracellular pH conditions. Since expression of TMPRSS2 appears to be highly
327 expressed in a subset of cells located in the nasopharyngeal cavity (*24*, *25*), we asked whether
328 this milieu would be acidic. Using a pH catheter placed in the left and right nasal cavities of 17
329 healthy male and female volunteers, we found a mildly acidic pH of around 6.6 (Fig. 4 E), in
330 agreement with earlier measurements (*26*, *27*).

DISCUSSION

We examined how SARS-CoV-2 Wuhan and its variants Delta and Omicron enter host cells using a combination of high-resolution live cell 3D imaging and quantitative assays for viral infectivity. Real-time tracking of single VSV-SARS-CoV-2 chimeric particles by lattice light sheet microscopy allowed us to visualize directly, with a sensitivity and time resolution substantially greater than any previous work, the key early steps of viral infection: virion binding, release of the S1-fragment upon cleavage by TMPRSS2, viral membrane fusion, and genome penetration into the cytosol. These observations revealed a previously unsuspected requirement to fuse by exposure to pH between 6.5 to 6.8, even after priming by TMPRSS2 and the attendant release of S1 and the S2' fragment (Figure 5).

Current understanding, derived in part from earlier work on SARS-CoV, has assumed that the only requirement for low pH was for cathepsin L activity when TMPRSS2 was absent or furin cleavage, a prerequisite for TMPRSS2 digestion, had failed during exit from the producing cell (*1*, *11*, *12*, *28–30*). Our results instead distinguish three complementary routes of productive entry, all of which involve exposure of the entering particle to pH < 6.8. The two principal routes are by uptake and traffic to early endosomes, for TMPRSS2-primed virions, or to late endosomal compartments, for cathepsin cleavage in cells regardless of the presence or absence of TMPRSS2. A third, minor route does not require virion uptake, but instead proceeds entirely at the cell surface, but only if cell attachment is at a pH range between 6.5 and 6.8. These observations define the alternative, multi-step pathways of SARS-CoV-2 entry and restrict the conditions for cell-surface penetration.

The released Atto 565-labeled fragment diffused laterally in the membrane, away from the labeled virion, consistent with our identification of the fragment as S1, which we expect to remain attached to ACE2. The release, which always preceded membrane fusion, was independent of exposure to acidic pH. Its dissociation was necessary but not sufficient for S2 to undergo its full, fusion-promoting conformational change. Release required S2' site cleavage, as evidenced by its absence in the presence of the TMPRSS2 inhibitor, Camostat, and by its absence, even in TMPRSS2 expressing cells, at pH lower than about 6.5, where TMPRSS2 is inactive. Trypsin cleavage in our experiments circumvented TMPRSS2 activity, and we indeed observed fusion at pH as low as 6.2.

364 The structure of the spike protein and the distribution of lysine residues suggest that most of the
365 Atto 565 label will be on S1 and hence, from the fraction of total label released, that about 25%
366 of the S-protein trimers will have shed S1 upon interaction with membrane bound ACE2,
367 assuming that dissociation of the 3 S1 fragments is cooperative. We estimate from the ratios of
368 stained band intensities on SDS-PAGE that the VSV chimeras have 15-20 S trimers on their
369 surface, and we infer from these numbers that on average, 3-4 spike will have lost S1, liberating
370 their S2 fragments to extend and interact with the host-cell membrane. This estimate is consistent
371 with the likely fraction of the virion surface that makes contact with the cell membrane and with
372 the dependence of S1 shedding from a trimer on its binding to ACE2. It is also consistent with the
373 number of active fusion proteins on other viruses, including VSV itself, required for fusion to
374 proceed (*31–34*).
375
376 Syncytium formation between cells expressing SARS-CoV-2 spike and cells expressing ACE2,
377 often used as a spike-mediated fusion assay, does not appear to depend upon acidic pH. But
378 the interface between the two cells will have vastly more spike protein than the interface between
379 a virus and a target cell. Thus, even low probability S1 dissociation events should be sufficient to
380 create a fusion pore, which can widen and spread across the entire cell-cell junction.
381
382 Release of S1 from a spike also detaches that spike from ACE2. Because cleavage at the S2'
383 site was complete in our experiments, any spike bound by ACE2 would probably have released
384 S1. Continued association with the host cell would thus have depended on formation of
385 alternative contacts as S1 dissociates. We propose that formation of an extended intermediate
386 and insertion of the S2 fusion peptides into the host-cell membrane creates the interactions that
387 retain the virion at the cell surface. This proposal further implies that protonation of one or more
388 S2 residues at acidic pH then enables S2 to collapse toward the folded-back, post fusion trimer
389 of hairpins and pull together the viral and host-cell lipid bilayers.
390
391 The Omicron variant is more refractory to furin cleavage than previously isolated strains. Its entry
392 pathway will thus depend on the level of furin activity in the producing cells. We indeed found
393 that when grown in Vero-TMPRSS2 cells, Omicron VSV chimeras were susceptible to S2'
394 cleavage by TMPRSS2 and entered from early endosomes or at the cell surface at mildly acidic
395 pH, but when grown in MA104 cells, they required cathepsin cleavage in late endosomes for
396 entry. With authentic SARS-CoV-2 virus, TMPRSS2 susceptibility similarly depended on the cells

397 in which the virus was propagated. These observations resolve some ambiguities in the literature
398 concerning the role of TMPRSS2 in Omicron infection (*35–37*).
399
400 Together with differential protease activities, the pH of respiratory mucosa could also influence
401 viral tropism. The pH of the airway-facing surface of the nasal cavity is between 6.2 and 6.8 (our
402 observations and (*26*). Thus, in principle, rapid entry could occur at the surface of TMPRSS2-
403 expressing cells in the nose. In other parts of the nasopharyngeal cavity and in the lung, the pH
404 is neutral (*38*), and we would not expect virus to fuse in those tissues until its endocytic uptake.
405
406 Our suggestion that at neutral pH, a relatively long-lived, extended S2 intermediate may be
407 present at the virus-cell interface bears both on potential therapeutic interventions and on the
408 availability of otherwise occluded epitopes to mucosal antibodies. Persistence of an extended
409 intermediate after gp120 release during HIV entry is thought to account for inhibition of viral
410 infectivity by the peptide fusion inhibitor entfuvirtide and for neutralization by antibodies that
411 recognize epitopes unavailable on a prefusion Env trimer. Our results are consistent with
412 observations that comparable interventions can impede SARS-CoV-2 infection in animal models
413 (*39*).

414 **MATERIAL AND METHODS**

415 **Materials and Cells**

416 All materials and cells used in this study are described in detail in Supplementary Appendix S1.

417

418 **Generation of VSV-SARS-CoV-2 chimeras**

419 The generation of a replication competent recombinant VSV chimera expressing eGFP where the
420 glycoprotein G was replaced with spike (S) protein Wuhan-Hu-1 strain (VSV-eGFP-SARS-CoV-
421 2) has been described (*13*). Additional details for the generation of the VSV recombinants
422 expressing eGFP and SARS-CoV-2 spike variants for Delta (B.1.617.2) and Omicron (B.1.1.529)
423 are described in Supplementary Appendix S1.

424

425 **Generation of SVG-A cells expressing ACE2 and TMPRSS2**

426 SVG-A cells ectopically expressing ACE2 and TMPRSS2 were generated by lentivirus
427 transduction. Briefly, lentivirus encoding human ACE2 or TMPRSS2 were generated as follows:
428 HEK293T packaging cells were seeded at 3.8×10^6 cells in a 10 cm tissue culture plate and grown
429 in complete DMEM supplemented with 10% v/v FBS at 37 °C and 5% CO_2.

430

431 Transfection mixtures containing 90 µL lipofectamine 3000 (Thermo Scientific L3000001),
432 psPAX2 (1.3 pmol; Addgene #12260), pMD2.G (0.72 pmol; Addgene #12259) and
433 TMPRSS2/pLX304 or ACE2/pLJM1 (1.64 pmol; gifts from Sean Whelan) 90 µL lipofectamine
434 3000 (Thermo Scientific L3000001), 1ul psPAX2 (1.3 pmol; Addgene #12260), 0.6 ul pMD2.G
435 (0.72 pmol; Addgene #12259) and 1.2 ul TMPRSS2/pLX304 or ACE2/pLJM1 (1.64 pmol) in 5 ml
436 OptiMEM medium (Thermo Scientific 31985062) mixed by pipetting and incubated for 20 minutes
437 at room temperature. 0.7 million cells were plated in a 10 cm plate 18 hr prior to transfection; the
438 medium was then replaced with the entire transfection mixture and cells incubated for 6 hours at
439 37°C, after which the medium was replaced with 15 ml complete DMEM medium. After 12 hours,
440 this medium was replaced with 15 ml of complete DMEM medium, which was then harvested 24
441 hr later after further growth. After addition of another 15 ml of medium, cells and virus were
442 allowed to growth, ending with a second harvest of medium. The medium was cleared of debris
443 by centrifugation at 5000 x g for 5 mins at room temperature and supernatants containing
444 lentivirus stored at -80°C.

445

446 Ectopic stably expression of ACE2 and TMPRSS2 was achieved by transduction of SVG-A cells
447 (gift from Walter J. Atwood, Brown University) gene-edited to simultaneously express

448 fluorescently tagged early and late endosomal markers EEA1 and NPC1 fused to mScarlett or
449 Halo, respectively (*21*). Briefly, SVG-A $1x10^6$ cells were seeded in a well from a 6-well plate and
450 grown overnight in MEM media with 10% FBS. Cleared medium containing ACE2 or TMPRSS2
451 lentivirus (1 mL) was added to the cells and incubated for 16 h, following replacement with fresh
452 medium cells were incubated for additional 24 hrs. Cells were allowed to grow for another 4 days
453 in the presence of 7 µg/mL puromycin to select for ACE2 expressing cells or 5 µg/mL blasticidin
454 for TMPRSS2 expressing cells. Surviving cells were grown in the absence of puromycin of
455 blasticidin for 4 days and cell stocks frozen and kept in liquid nitrogen. SVG-A cells
456 simultaneously stably expressing ACE2 and TMPRSS2 were obtained by transduction with
457 lentivirus encoding TMPRSS2 and selection with Blasticidin of cells stably expressing ACE2.
458
459 **Preparation of VSV chimeras for imaging and infection experiments**
460 All VSV-SARS-CoV-2 variants were grown in MA104 cells in 15 to 20 150-mm dishes and infected
461 at a multiplicity of infection (MOI) of 0.01 as previously described (*9*, *13*) in addition to the Omicron
462 variant also grown in Vero TMPRSS2 cells. Briefly, media containing the viruses were collected
463 72 hours post infection and clarified by centrifugation at 1,000 x g for 10 min at 4°C. A pellet with
464 virus and extracellular particles was obtained by centrifugation in a Ti45 fixed-angle rotor at
465 72,000 x g (25,000 rpm) for 2 hours at 4°C, then resuspended overnight in 0.5 mL PBS at 4°C.
466 This solution was layered on top of a 15% sucrose-PBS solution and a pellet with virions obtained
467 by centrifugation in a SW55 swinging-bucket rotor at 148,000 x g (35,000 rpm) for 2 hours at 4°C.
468 The resulting pellet was resuspended overnight in 0.4 mL PBS at 4°C, layered on top of a 15 to
469 45% sucrose-PBS linear gradient and subjected to centrifugation in a SW55 swinging-bucket rotor
470 at 194,000 x g (40,000 rpm) for 1.5 hours at 4°C. The predominant light scattering band located
471 in the lower one-third of the gradient and containing the virions was removed by side puncture of
472 the gradient tube. Approximately 0.3 ml of this solution was mixed with 25 ml of PBS and
473 subjected to centrifugation in a Ti60 fixed-angle rotor at 161,000 x g (40,000 rpm) for 2 hours at
474 4°C. The final pellet was resuspended overnight in 0.2 - 0.5 mL PBS aliquoted and stored frozen
475 at -80°C for use in subsequent imaging and infection experiments, without detectable change in
476 infectivity.
477
478 **Isolation and propagation of SARS-CoV-2**
479 A human isolate of SARS-CoV-2, Wuhan (B.1) was obtained in accordance with the protocol
480 approved by the Helsinki University Hospital laboratory research permit 30 HUS/32/2018§16.
481 Briefly, a nasopharyngeal swabs from a patient infected with COVID19 was suspended in 0.5 ml

482 of universal transport medium (UTM®, Copan Diagnostics) and used to inoculate Vero TMPRSS2*
483 cells for 1 h at 37°C, after which the inoculum was replaced with minimum essential medium
484 (MEM) supplemented with 2% heat inactivated FBS, L-glutamine, penicillin, and streptomycin and
485 virus allowed to grow for 48 hr. Virions in the supernatant (P0) were subjected to a similar second
486 round of propagation (P1), analyzed by DNA sequencing, and aliquots stored at 80°C in a solution
487 containing MEM, 2% heat inactivated FCS, 2 mM L-glutamine, and 1% penicillin-streptomycin.
488 Extent of virus replication was determined by real-time PCR (RT-PCR) using primers for SARS-
489 CoV-2 RNA-dependent RNA polymerase (RdRP) (*40*).
490
491 **VSV-eGFP-SARS-CoV-2 infection assays**
492 Infection assays for the Wuhan, Delta or Omicron VSV-eGFP-SARS-CoV-2 chimeras were done
493 at a final ~ 80% confluency of cells plated one day before the infection assay as previously
494 described (*9*) and further explained in Supplementary Appendix S1.
495
496 **SARS-CoV-2 infection assays**
497 All experiments with SARS-CoV-2 were performed in biosafety level 3 (BSL3) facilities at the
498 University of Helsinki with appropriate institutional permits. Virus samples were obtained under
499 Helsinki University Hospital laboratory research permit 30 HUS/32/2018§16. Infections were
500 carried for 16 hours at 37°C with 5% CO_2. Cells were then fixed with 4% paraformaldehyde in
501 PBS for 30 min at room temperature before being processed for immunodetection of viral N
502 protein, automated fluorescence imaging, and image analysis. The detailed protocol is outlined in
503 the Supplementary Appendix S1.
504
505 **VSV-SARS-CoV-2 Atto 565 labeling and single molecule Atto 565 dye calibration**
506 Stock solutions of VSV-SARS-CoV-2 and its variants at a concentration of ~150 µg/ml viral RNA
507 were conjugated with Atto 565-NHS ester (Sigma-Aldrich, cat. 72464) as previously described
508 (*41*). The number of Atto 565 molecules attached to a single virion was determined by comparing
509 the total fluorescence intensities associated with a given virion and the fluorescence intensity
510 associated with the last bleaching step of the same virion, as previously described (*42*, *43*). A
511 brief description of these steps are outlined in the Supplementary Appendix S1.
512
513 **Trypsin cleavage of VSV-eGFP-SARS-CoV-2**
514 VSV-eGFP-SARS-CoV-2 and variants (as indicated in text) at a concentration 30 µg/mL virus
515 RNA in a total volume of 100 µL in DMEM with 25 mM HEPES, pH 7.4 were incubated for 30 min

516 at 37°C with 1 µg/mL trypsin (Pierce trypsin, TPCK treated from Thermo scientific cat. PI20233).
517 Trypsin activity was terminated with 10 µM Aprotinin (bovine lung, Sigma-Aldrich cat. A1153). The
518 required concentration of trypsin was determined by trypsin serial dilution, aiming for the largest
519 infectivity Vero cells whose endogenous cathepsin proteases activity had been inhibited with 20
520 µM E-64 (Figure S19). Infections were done with VSV or its variants at a concentration of 0.5
521 µg/mL (for Vero and Vero TMPRSS2) or 5 µg/mL virus RNA (for Caco-2 or Calu-3). When
522 required, the trypsin cleaved VSV's were used together with infection inhibitors or for pH bypass
523 experiments as described above.
524
525 ***In vitro* release of S1 from trypsin activated VSV-SARS-CoV-2**
526 VSV-eGFP-SARS-CoV-2-Atto 565 was incubated with trypsin at various concentrations for 30
527 min and the reaction stopped by addition of aprotinin to a final concentration of 10 µM. Virus was
528 then used to infect Vero cells with endogenous cathepsin proteases inhibited with 20 µM E-64 to
529 determine maximum concentration of trypsin required to proteolytically activate the virus. Virus
530 either without or with trypsin cleavage, or with ACE2 bound before and after trypsin cleavage
531 were plated onto a poly-D-lysine coated glass to determine the number of Atto 565 fluorescence
532 dyes associated with each one of the single particles using spinning disc confocal microscopy. At
533 least 8,000 particles were imaged per experimental condition to guarantee the ability to distinguish
534 intensity losses of at least 20%. Every experimental condition was repeated in triplicate and the
535 intensity of the mean intensities of the peak Gaussian fit was used to determine the after and
536 deviation of Atto565 dyes per condition, Figure S19.
537
538 A computation simulation was performed to validate the ability to detect with statistical
539 significance a 20% fluorescence intensity loss approximate equivalent to the 20-30% loss
540 observed *in vivo* with virions when attached to the cell surface of Vero TMPRSS2. Experimental
541 data corresponding to 8,845 undigested control virions were used to generate a probability density
542 function from which 9 fit parameters (3 mean intensities with corresponding sigmas and the
543 relative contribution to the distribution) were obtained by fitting the sum of 3 Gaussian
544 distributions. These parameters were then used to generate 8845 random numbers of the same
545 distribution and compared to the experimental data set to illustrate the accuracy of the simulation.
546 A second set of 8845 random numbers were generated with mean intensities reduced by 20%, to
547 generate a probability density distribution representing the fluorescence intensities after ACE2
548 mediated release of S cleavage by TMPRSS2.
549

550 **Nasal pH and temperature measurements**

551 The pH and temperature of the nasal cavity, close to the under lower turbinate, from each nostril
552 from 17 healthy volunteers, age 26-55, males and females, were determined using a Digitrapper
553 pH 400 recorder (Medtronic) connected to a single-use Versaflex disposal dual sensor pH
554 catheter (Medtronic) and a Beurer FT 15/1digital thermometer (Beurer), respectively. The
555 temperature dependent pH response of the Digtrapper was corrected to consider the temperature
556 in the nostrils determined for each volunteer.

557

558 These measurements were obtained under the ethical permit n. HUS/2502/2020 granted by the
559 ethical committee of Helsinki and Uusimaa hospital district to Ahmed Geneid and Markku Patjas
560 at the Helsinki University Hospital.

561

562 **Preparation of glass coverslips**

563 Infection and uptake assays of VSV-eGFP-SARS-CoV-2 and VSV-P-eGFP-SARS-CoV-2 done
564 by spinning disc confocal microscopy visualization, were performed using 25 mm #1.5 coverslips
565 bound with polydimethylsiloxane (PDMS) of about 1 mm in thickness and of 3 mm (infection) or
566 5 mm (uptake) in diameter wells punched as previously described (*9*) (see also in Supplementary
567 Appendix S1).

568

569 **Live cell spinning disc-confocal microscopy**

570 Visualization experiments were done with an inverted spinning disc confocal microscope (*42*)
571 following the details described in Supplementary Appendix S1.

572

573 **Live cell lattice light sheet microscopy**

574 Cells were plated in a 35 mm culture dish containing 5 mm in diameter glass coverslips to achieve
575 60% final confluency the day of each experiment. Immediately before lattice light sheet
576 visualization, the cover slip was placed on top of parafilm placed in a 10 cm in diameter petri dish
577 including wet chem wipes to maintain humidity. Approximately 10 µL of a solution containing VSV-
578 SARS-CoV-2 in DMEM with 25 mM HEPES at pH 7.4 for the times indicated in the text, after
579 which the coverslips were transferred to the imaging stage of the LLSM. Visualization was done
580 using phenol red free media, (FluoroBrite™) supplemented with 5% FBS and 25 mM HEPES at
581 the indicated pH. Imaging was done at 37°C in the presence of 5% CO_2 and 100 nM fluorescent
582 Alexa 647 or Alexa 549 dyes added to the medium to determine the cell boundary. The LLSM
583 was operated in sample scan mode with 0.5 µm spacing between each plane along the z-imaging

584 axis and samples imaged as a time series of stacks acquired 1 to 5 sec using dithered multi-
585 Bessel lattice light sheet illumination (*40*, *43*). When using gene edited SVG-A cells expressing
586 EEA1-Scarlett and NPC1-Halo, Halo was first labeled by incubation of the cells with 200 nM
587 JFX646 for 30 minutes at 37ºC and 5% CO_2 followed by three 2-minute washes with DMEM
588 containing 10% FBS, 25 mM HEPES, pH 7.4 within 2 hours prior to virus addition to the cover
589 slip. Time series containing 120-300 z-stacks, sequentially obtained every 1-5 sec were acquired
590 with ~ 10 ms exposures per channel.
591
592 The following protocol was used to determine the dwell time between binding of trypsin activated
593 VSV-SARS-CoV-2-Atto 565 Wuhan and release of the S-fragment. Briefly, trypsin activated
594 virions at 5 µg/mL viral RNA were flowed on top of Vero cells plated in a homemade microfluidic
595 flow cell one day prior to the experiment to achieve a 90% confluency. Soluble 100 nM Alexa 549
596 added to the medium was used to determine the cell outline. Samples were imaged with an AO-
597 LLSM microscope configured for sample scan imaging to acquire every 4 sec a stack with planes
598 separated by 0.6 um (0.3 um along the z-optical axis) using an exposure of 3 ms/plane.
599
600 **Single virus tracking and image analysis**
601 The 3D stacks obtained using LLSM were deskewed and the diffraction limited spots were
602 detected and tracked in three dimensions using the automated detection algorithms that uses
603 least-squares minimization numerical fitting with a model of the microscope PSF approximated
604 by a 3D Gaussian function and implemented using the MATLAB developed previously (*40*)
605 available for download (https://github.com/VolkerKirchheim/TrackBrowser_Matlab.git).
606 Estimated fluorescent intensities associated with each spot were calculated from the
607 corresponding amplitudes of the fitted 3D Gaussian and compared to those from single virions
608 bound to poly-D-lysine coated glass imaged under the same acquisition conditions and whose
609 dye content was determined by single bleaching steps (*43*).
610
611 Tracks with intensities corresponding to single virus were exported into a custom-made program
612 written in LabView for visualizing trajectories available for download
613 (https://github.com/VolkerKirchheim/TrackBrowser_LabView.git). Each virus trajectory was
614 visually examined for co-localization within a specific compartment (cell surface, EEA1 early
615 endosomes or NPC-1 late endosomes/lysosomes, cytosol) and the mean squared displacements
616 (MSDs) were calculated from all 3D coordinates for all possible time frames within that

compartment. A non-linear relationship between MSD and time for anomalous diffusion was fitted to the MSD data according to the power law in equation:

$$MSD(t) = 6\,K\,t^{\alpha}$$

where *K* is the generalized diffusion coefficient and α is the anomalous exponent.

Statistical analysis

An unpaired t-test was used to determine the statistical significance in the difference between control and experimental values.

625 **FIGURE LEGENDS:**

626 **Figure 1**. **SARS-CoV-2 infection requires endocytosis**

627 **(A)** Schematic of live-cell volumetric lattice-light-sheet fluorescence microscopy (LLSM) imaging
628 experiments **(B-G)** used to obtain 3D time series of VSV-eGFP-P-SARS-CoV-2-S-Atto 565 entry
629 into VERO TMPRSS2 cells during early stages of infection using an MOI of 2. For each
630 experiment, three cells were consecutively imaged volumetrically every 4.7 seconds for 10 min.

631 **(B)** Maximum intensity projections showing fluorescently tagged VSV-SARS-CoV-2 within 1 um
632 in thickness optical sections from the first frame of the time series acquired for representative
633 cells 1, 2 and 3.

634 **(C)** Representative single virion trajectories of VSV-eGFP-P-SARS-CoV-2-S-Atto 565 within a 1
635 um optical slice of a time series acquired during the first 10-minutes of cell 1. Traces highlight
636 particles at the cell surface (black) and within the cell volume after endocytosis (blue), in both
637 cases containing colocalized eGFP-P and S-Atto 565; it also shows traces in the cytosol (green)
638 containing eGFP-P upon its separation from the Atto565 signal (light blue). Single images
639 highlighting these events are shown in the panels below.

640 **(D)** Orthogonal projection of the traced event highlighted in **(C)**.

641 **(E)** Representative summary of 266 virion traces analyzed during cell entry. Data from single
642 coverslips (out of five) obtained per each cell type are shown. Vertical traces highlight the transfer
643 of virions from the cell surface to the cell interior (assumed to be in endosomes because the
644 colocalization of the eGFP-P with S-Atto 565 signals) or from endosomes to the cytosol (upon
645 loss of localization of the eGFP-P and S-Atto 565 signals). Events corresponding to step wise
646 loss of the S-Atto 565 signal at the cell surface are indicated (yellow).

647 **(F)** Representative plot illustrating the mean squared displacements (MSD) for the trajectory
648 depicted in **(D)** when the particle is at the cell surface (black), in endosomes (blue), or in the
649 cytosol upon separation of eGFP-P (which remains in endosomes, light blue) and S-Atto565 in
650 the cytosol (green).

651 **(G)** Summary dot plot showing the diffusion mode (α) for 1692 virion trajectories and
652 corresponding 139 penetration events; all penetration events occurred from endosomes except
653 for one event at the cell surface in a single Vero TMRSS2 cell. The plot highlights the confined
654 motion ($\alpha < 0.80$) of virions at the cell surface, trajected motion ($\alpha > 1.2$) in endosomes, and
655 Brownian motion ($0.80 < \alpha < 1.2$) in the cytosol.

656 **(H-J)** Effect of inhibition of endocytosis in the infection by VSV-eGFP-SARS-CoV-2 **(H,I)** or a
657 human isolate of SARS-CoV-2 **(J)**. Top panel shows examples of infection observed in
658 representative fields of Vero TMPRSS2 over expressing or not the dominant negative dynamin

659 K44A mutant or treated or not with 40 μM dynasore-OH. Images in the top panels were obtained
660 using spinning disc confocal microscopy and show maximum intensity projections. Results from
661 similar infections obtained with different cell types are shown in the bottom panel. The difference
662 of results between control conditions and inhibition of endocytosis by K44A dynamin
663 overexpression or incubation with dynasore-OH incubation was statistically significant with p
664 value of <0.001 using an unpaired t-test.
665
666 **Figure 2. Endocytic entry routes of VSV-SARS-CoV-2.** VSV-eGFP-P-SARS-CoV-2 was used
667 to infect SVG-A gene-edited to express early endosomal antigen 1 fused to the fluorescent protein
668 Scarlet (EEA1-Scarlett) as an early endosomal marker and for late endosomal/lysosomal
669 compartments a Halo-tagged version of the cholesterol transporter Niemann Pick C1 (NPC1-
670 Halo) together with ectopic expression of ACE2 and TMPRSS2 and volumetrically imaged using
671 LLSM according to Fig. 1.
672 **(A)** Representative 2 μm projection from the first frame of the time series acquired 8-min after
673 inoculation.
674 **(B-E)** Representative examples of single trajectories of VSV-eGFP-P-SARS-CoV-2 highlighting
675 the extent of colocalization between eGFP-P and EEA1 or between eGFP-P and NPC-1 Halo
676 labeled with JFX646 (top panel), the orthogonal projection of the trajectory (middle panel) and
677 corresponding plots for number of VSV particles on the spot, extent of colocalizations and MSD
678 (bottom panels). Additional examples found in related Fig S11-16.
679 **(F)** Representative summary of results for 257 and 373 virion traces analyzed during cell entry
680 from single coverslips (out of a total of five) plated with SVG-A ACE2 or SVG-A ACE2 TMPRSS2.
681 Vertical and diagonal traces highlight the transfer of virions from the cell surface to its interior and
682 associated with early or late endosomes/lysosomes as defined by colocalization of eGFP-P with
683 EEA1-Scarlett or eGFP-P with NPC1-Halo, respectively.
684
685 **Figure 3. Surface entry route of SARS-CoV-2**
686 **(A-G)** VSV-eGFP-P-SARS-CoV-2-S-Atto 565 was used to infect Vero TMPRSS2 cells and used
687 to study the effect by acidic pH in the medium on the TMPRSS2 mediated surface release of the
688 S-fragment, on cellular location of fusion and genome delivery and on infectivity.
689 **(A, B)** Single virion trajectories of VSV-eGFP-P-SARS-CoV-2-Atto565 in a Vero TMPRSS2 cell
690 incubated at pH 6.8 showing in **(A)** an example of S-release at the surface without subsequent
691 fusion and **(B)** an example of S-release followed by penetration of eGFP-P to the cytosol.

692 Orthogonal views of the tracings and corresponding time-dependent fluorescent intensities for S-
693 Atto 565 and eGFP-P are shown.
694 **(C)** Representative summary from 237 virion traces analyzed during cell entry. Data from single
695 coverslips (out of five) obtained per each pH condition in the medium are shown. Vertical traces
696 of cells incubated at 6.8 highlight the efficient transfer of virions from the cell surface to the cell
697 interior (based on loss of signal colocalization between eGFP-P and S-Atto 565 and
698 corresponding change of diffusion from constrained to directed). Events of stepwise partial loss
699 of S-Atto 565 are indicated (yellow). Similar data with cells incubated at pH 6.2 shows
700 accumulation of virions in endosomes, complete absence of fusion events from the cell surface
701 and limited number of fusion events from endosomes.
702 **(D)** Data showing fraction of virions that released the S-fragment from virions at the cell surface
703 of Vero TMPRSS2 cells incubated at pH 6.8 in the absence or presence of 10 uM Camostat, or
704 of Vero E6, Caco-2 or Calu-3 cells also at pH 6.8 and in the absence of Camostat. The difference
705 of results between control and all other conditions was statistically significant with p value of
706 <0.0001 using an unpaired t-test.
707 **(E)** Cumulative plot corresponding to the dwell time between the stepwise partial drop of the S-
708 Atto 565 signal of a virion at the cell surface and fusion defined by surface spreading of the
709 remaining Atto 565 signal and transfer into the cytosol of eGFP-P. Data from 86 traces and from
710 five experiments.
711 **(F)** Effect of extracellular pH on the transfer of eGFP-P of virions from the cell surface (red) or
712 from endosomes (black) to the cytosol. Each dot represents average +/- std from 5 coverslips
713 with 3 cells imaged per coverslip and at least 600 virus tracked per condition. Line across box
714 represents the median of distribution and the top and bottom represent the quartiles.
715 **(G)** Effect of extracellular pH of the cell medium on the mode of diffusion of the eGFP-P signal
716 associated with a virion before and after delivery from the surface (red) or from endosomes (black)
717 to the cytosol.
718 **(H)** pH bypass infection experiments to test the effect of extracellular acidic pH on the extent of
719 infection of Vero or Vero TMPRSS2 cells by VSV-eGFP-SARS-CoV-2 alone or treated for 30 min
720 with 1 µg/mL trypsin; experiments carried in the absence (top panel) or presence (middle and
721 bottom panels) of 40 uM dynasore-OH. Each data point represents an experiment. In each case,
722 the values determined at pH 6.8 and 7.4 are significantly different with a p value of at least <0.0003
723 using an unpaired t-test.
724 **(I)** pH bypass infection experiment using authentic SARS-CoV-2 and Vero TMPRSS2* cells in the
725 absence or presence of 40 uM dynasore-OH. Each data point represents an experiment. No

726 statistical difference was observed in the absence of dynasore-OH between pH 6.8 and pH 7.4
727 ($p = 0.13$); the difference was statistically significant in the presence of dynasore-OH ($p < 0.0001$)
728 using an unpaired t-test.
729
730 **Figure 4. Entry routes of VSV-SARS-CoV-2 variants are conserved.**
731 **(A-C)** Effect of extracellular pH and type of cells infected with the indicated variants of VSV-eGFP-
732 P-SARS-CoV-2 on **(A)** the extent of S-fragment release from the cell surface and of **(B)** fusion
733 from the cell surface or **(C)** from endosomes.
734 **(D)** Experiments to determine the effect of extracellular pH on the extent of infection by the Delta
735 and Omicron variants of VSV-SARS-CoV-2 in the presence of 40 uM dynasore-OH. The pH
736 bypass experiments in the right panel were done with trypsin-cleaved virions. The bottom two
737 rows compare results obtained with the Omicron variant grown in MA104 or Vero TMPRSS2 cells.
738 Western Blot showing cleavage states of spike protein of VSV-SARS-CoV-2-Omicron grown in
739 different cell types. The bypass pH experiments in the left panels show statistical differences
740 between pH 6.8 and pH 7.4 ($p < 0.0001$) for Delta and Omicron grown in Vero TMPRRSS2 and
741 of minimal significance for Omicron grown MA 104 using an unpaired t-test. Similar analysis for
742 the experiments in the right panels show statistical differences between pH 6.8 and pH 7.4 for
743 Delta ($p < 0.0001$) and Omicron grown in Vero TMPRRSS2 ($p < 0.0001$) and also for Omicron (P
744 $= 0.0015$) grown in MA 104.
745 **(E)** Nasal pH values determined from 17 healthy individuals. Each dot represents a single pH
746 determination by the pH catheter at the lower turbinate of the right and left nostrils.
747
748 **Figure 5. Schematic representation of the principal entry routes SARS-CoV-2 uses for**
749 **infection.** Entry starts with membrane attachment and ends with spike-protein (S) catalyzed
750 membrane fusion releasing the viral contents into the cytosol. Fusion activity depends on two
751 proteolytic cleavage steps, one typically carried out by furin in the producing cell and the second
752 by TMPRSS2 on the cell surface on in endosomes of the target cell. Alternatively, endosomal
753 cathepsins can carry out both cleavages. Exposure of the virus to an acidic milieu is essential for
754 membrane fusion, genome penetration, and productive infection. Fusion and penetration occur
755 only in acidic early and late endosomal/lysosomal compartments but not at the cell surface, even
756 when the furin and TMPRSS2 cleavages have both occurred. Fusion and penetration can occur
757 at the cell surface of cells expressing TMPRSS2 if the extracellular pH is ~6.8.
758

759 **REFERENCES**

760

761 1. M. Hoffmann, H. Kleine-Weber, S. Schroeder, N. Krüger, T. Herrler, S. Erichsen, T. S.
762 Schiergens, G. Herrler, N.-H. Wu, A. Nitsche, M. A. Müller, C. Drosten, S. Pöhlmann, SARS-
763 CoV-2 Cell Entry Depends on ACE2 and TMPRSS2 and Is Blocked by a Clinically Proven
764 Protease Inhibitor. *Cell*. 181, 271-280.e8 (2020).

765 2. D. Wrapp, N. Wang, K. S. Corbett, J. A. Goldsmith, C.-L. Hsieh, O. Abiona, B. S. Graham, J.
766 S. McLellan, Cryo-EM structure of the 2019-nCoV spike in the prefusion conformation. *Science*.
767 367, 1260–1263 (2020).

768 3. J. Yang, S. J. L. Petitjean, M. Koehler, Q. Zhang, A. C. Dumitru, W. Chen, S. Derclaye, S. P.
769 Vincent, P. Soumillion, D. Alsteens, Molecular interaction and inhibition of SARS-CoV-2 binding
770 to the ACE2 receptor. *Nat Commun*. 11, 4541 (2020).

771 4. R. Yan, Y. Zhang, Y. Li, L. Xia, Y. Guo, Q. Zhou, Structural basis for the recognition of SARS-
772 CoV-2 by full-length human ACE2. *Sci New York N Y*. 367, 1444–1448 (2020).

773 5. J. Shang, Y. Wan, C. Luo, G. Ye, Q. Geng, A. Auerbach, F. Li, Cell entry mechanisms of
774 SARS-CoV-2. *P Natl Acad Sci Usa*. 117, 11727–11734 (2020).

775 6. C. B. Jackson, M. Farzan, B. Chen, H. Choe, Mechanisms of SARS-CoV-2 entry into cells.
776 *Nat Rev Mol Cell Biology*. 23, 3–20 (2022).

777 7. B. A. Johnson, X. Xie, A. L. Bailey, B. Kalveram, K. G. Lokugamage, A. Muruato, J. Zou, X.
778 Zhang, T. Juelich, J. K. Smith, L. Zhang, N. Bopp, C. Schindewolf, M. Vu, A. Vanderheiden, E.
779 S. Winkler, D. Swetnam, J. A. Plante, P. Aguilar, K. S. Plante, V. Popov, B. Lee, S. C. Weaver,
780 M. S. Suthar, A. L. Routh, P. Ren, Z. Ku, Z. An, K. Debbink, M. S. Diamond, P.-Y. Shi, A. N.
781 Freiberg, V. D. Menachery, Loss of furin cleavage site attenuates SARS-CoV-2 pathogenesis.
782 *Nature*. 591, 293–299 (2021).

783 8. R. Zang, M. F. G. Castro, B. T. McCune, Q. Zeng, P. W. Rothlauf, N. M. Sonnek, Z. Liu, K. F.
784 Brulois, X. Wang, H. B. Greenberg, M. S. Diamond, M. A. Ciorba, S. P. J. Whelan, S. Ding,
785 TMPRSS2 and TMPRSS4 promote SARS-CoV-2 infection of human small intestinal
786 enterocytes. *Sci Immunol*. 5, eabc3582 (2020).

787 9. A. J. B. Kreutzberger, A. Sanyal, R. Ojha, J. D. Pyle, O. Vapalahti, G. Balistreri, T.
788 Kirchhausen, Synergistic Block of SARS-CoV-2 Infection by Combined Drug Inhibition of the
789 Host Entry Factors PIKfyve Kinase and TMPRSS2 Protease. *J Virol*. 95, e0097521 (2021).

790 10. X. Ou, Y. Liu, X. Lei, P. Li, D. Mi, L. Ren, L. Guo, R. Guo, T. Chen, J. Hu, Z. Xiang, Z. Mu,
791 X. Chen, J. Chen, K. Hu, Q. Jin, J. Wang, Z. Qian, Characterization of spike glycoprotein of
792 SARS-CoV-2 on virus entry and its immune cross-reactivity with SARS-CoV. *Nat Commun*. 11,
793 1620 (2020).

794 11. T. P. Peacock, D. H. Goldhill, J. Zhou, L. Baillon, R. Frise, O. C. Swann, R. Kugathasan, R.
795 Penn, J. C. Brown, R. Y. Sanchez-David, L. Braga, M. K. Williamson, J. A. Hassard, E. Staller,
796 B. Hanley, M. Osborn, M. Giacca, A. D. Davidson, D. A. Matthews, W. S. Barclay, The furin

797 cleavage site in the SARS-CoV-2 spike protein is required for transmission in ferrets. *Nat*
798 *Microbiol*. 6, 899–909 (2021).

799 12. D. Bestle, M. R. Heindl, H. Limburg, T. V. L. van, O. Pilgram, H. Moulton, D. A. Stein, K.
800 Hardes, M. Eickmann, O. Dolnik, C. Rohde, H.-D. Klenk, W. Garten, T. Steinmetzer, E.
801 Böttcher-Friebertshäuser, TMPRSS2 and furin are both essential for proteolytic activation of
802 SARS-CoV-2 in human airway cells. *Life Sci Alliance*. 3, e202000786 (2020).

803 13. J. B. Case, P. W. Rothlauf, R. E. Chen, Z. Liu, H. Zhao, A. S. Kim, L.-M. Bloyet, Q. Zeng, S.
804 Tahan, L. Droit, Ma. X. G. Ilagan, M. A. Tartell, G. Amarasinghe, J. P. Henderson, S. Miersch,
805 M. Ustav, S. Sidhu, H. W. Virgin, D. Wang, S. Ding, D. Corti, E. S. Theel, D. H. Fremont, M. S.
806 Diamond, S. P. J. Whelan, Neutralizing Antibody and Soluble ACE2 Inhibition of a Replication-
807 Competent VSV-SARS-CoV-2 and a Clinical Isolate of SARS-CoV-2. *Cell Host Microbe*. 28,
808 475-485.e5 (2020).

809 14. B.-C. Chen, W. R. Legant, K. Wang, L. Shao, D. E. Milkie, M. W. Davidson, C.
810 Janetopoulos, X. S. Wu, J. A. H. III, Z. Liu, B. P. English, Y. Mimori-Kiyosue, D. P. Romero, A.
811 T. Ritter, J. Lippincott-Schwartz, L. Fritz-Laylin, R. D. Mullins, D. M. Mitchell, J. N. Bembenek,
812 A.-C. Reymann, R. Böhme, S. W. Grill, J. T. Wang, G. Seydoux, U. S. Tulu, D. P. Kiehart, E.
813 Betzig, Lattice light-sheet microscopy: Imaging molecules to embryos at high spatiotemporal
814 resolution. *Science*. 346, 1257998 (2014).

815 15. C. J. Bradish, J. B. Kirkham, The Morphology of Vesicular Stomatitis Virus (Indiana C)
816 Derived from Chick Embryos or Cultures of BHK21/13 Cells. *Microbiology*+. 44, 359–371
817 (1966).

818 16. D. K. Cureton, R. H. Massol, S. P. J. Whelan, T. Kirchhausen, The Length of Vesicular
819 Stomatitis Virus Particles Dictates a Need for Actin Assembly during Clathrin-Dependent
820 Endocytosis. *Plos Pathog*. 6, e1001127 (2010).

821 17. J. Klumperman, G. Raposo, The Complex Ultrastructure of the Endolysosomal System. *Csh*
822 *Perspect Biol*. 6, a016857 (2014).

823 18. S. M. Ferguson, P. D. Camilli, Dynamin, a membrane-remodelling GTPase. *Nat Rev Mol*
824 *Cell Bio*. 13, 75–88 (2012).

825 19. H. Damke, T. Baba, D. E. Warnock, S. L. Schmid, Induction of mutant dynamin specifically
826 blocks endocytic coated vesicle formation. *J Cell Biology*. 127, 915–934 (1994).

827 20. E. Macia, M. Ehrlich, R. Massol, E. Boucrot, C. Brunner, T. Kirchhausen, Dynasore, a Cell-
828 Permeable Inhibitor of Dynamin. *Dev Cell*. 10, 839–850 (2006).

829 21. Y.-L. Kang, Y. Chou, P. W. Rothlauf, Z. Liu, T. K. Soh, D. Cureton, J. B. Case, R. E. Chen,
830 M. S. Diamond, S. P. J. Whelan, T. Kirchhausen, Inhibition of PIKfyve kinase prevents infection
831 by Zaire ebolavirus and SARS-CoV-2. *Proc National Acad Sci*. 117, 20803–20813 (2020).

832 22. R. Zang, J. B. Case, E. Yutuc, X. Ma, S. Shen, M. F. G. Castro, Z. Liu, Q. Zeng, H. Zhao, J.
833 Son, P. W. Rothlauf, A. J. B. Kreutzberger, G. Hou, H. Zhang, S. Bose, X. Wang, M. D. Vahey,
834 K. Mani, W. J. Griffiths, T. Kirchhausen, D. H. Fremont, H. Guo, A. Diwan, Y. Wang, M. S.

835 Diamond, S. P. J. Whelan, S. Ding, Cholesterol 25-hydroxylase suppresses SARS-CoV-2
836 replication by blocking membrane fusion. *P Natl Acad Sci Usa*. 117, 32105–32113 (2020).

837 23. S. Belouzard, V. C. Chu, G. R. Whittaker, Activation of the SARS coronavirus spike protein
838 via sequential proteolytic cleavage at two distinct sites. *Proc National Acad Sci*. 106, 5871–5876
839 (2009).

840 24. Y. Liu, H.-Q. Qu, J. Qu, L. Tian, H. Hakonarson, Expression Pattern of the SARS-CoV-2
841 Entry Genes ACE2 and TMPRSS2 in the Respiratory Tract. *Viruses*. 12, 1174 (2020).

842 25. S. P. Sajuthi, P. DeFord, Y. Li, N. D. Jackson, M. T. Montgomery, J. L. Everman, C. L. Rios,
843 E. Pruesse, J. D. Nolin, E. G. Plender, M. E. Wechsler, A. C. Y. Mak, C. Eng, S. Salazar, V.
844 Medina, E. M. Wohlford, S. Huntsman, D. A. Nickerson, S. Germer, M. C. Zody, G. Abecasis, H.
845 M. Kang, K. M. Rice, R. Kumar, S. Oh, J. Rodriguez-Santana, E. G. Burchard, M. A. Seibold,
846 Type 2 and interferon inflammation regulate SARS-CoV-2 entry factor expression in the airway
847 epithelium. *Nat Commun*. 11, 5139 (2020).

848 26. R. J. A. England, J. J. Homer, L. C. Knight, S. R. Ell, Nasal pH measurement: a reliable and
849 repeatable parameter. *Clin Otolaryngology Allied Sci*. 24, 67–68 (1999).

850 27. B.-G. Kim, J.-H. Kim, S.-W. Kim, S.-W. Kim, K.-S. Jin, J.-H. Cho, J.-M. Kang, S.-Y. Park,
851 Nasal pH in patients with chronic rhinosinusitis before and after endoscopic sinus surgery. *Am J*
852 *Otolaryng*. 34, 505–507 (2013).

853 28. I. Glowacka, S. Bertram, M. A. Müller, P. Allen, E. Soilleux, S. Pfefferle, I. Steffen, T. S.
854 Tsegaye, Y. He, K. Gnirss, D. Niemeyer, H. Schneider, C. Drosten, S. Pöhlmann, Evidence that
855 TMPRSS2 Activates the Severe Acute Respiratory Syndrome Coronavirus Spike Protein for
856 Membrane Fusion and Reduces Viral Control by the Humoral Immune Response. *J Virol*. 85,
857 4122–4134 (2011).

858 29. G. Simmons, S. Bertram, I. Glowacka, I. Steffen, C. Chaipan, J. Agudelo, K. Lu, A. J.
859 Rennekamp, H. Hofmann, P. Bates, S. Pöhlmann, Different host cell proteases activate the
860 SARS-coronavirus spike-protein for cell–cell and virus–cell fusion. *Virology*. 413, 265–274
861 (2011).

862 30. J. K. Millet, G. R. Whittaker, Host cell entry of Middle East respiratory syndrome coronavirus
863 after two-step, furin-mediated activation of the spike protein. *Proc National Acad Sci*. 111,
864 15214–15219 (2014).

865 31. D. L. Floyd, J. R. Ragains, J. J. Skehel, S. C. Harrison, A. M. van Oijen, Single-particle
866 kinetics of influenza virus membrane fusion. *Proc National Acad Sci*. 105, 15382–15387 (2008).

867 32. T. Ivanovic, J. L. Choi, S. P. Whelan, A. M. van Oijen, S. C. Harrison, Influenza-virus
868 membrane fusion by cooperative fold-back of stochastically induced hemagglutinin
869 intermediates. *Elife*. 2, e00333 (2013).

870 33. L. H. Chao, D. E. Klein, A. G. Schmidt, J. M. Peña, S. C. Harrison, Sequential
871 conformational rearrangements in flavivirus membrane fusion. *Elife*. 3, e04389 (2014).

872 34. I. S. Kim, S. Jenni, M. L. Stanifer, E. Roth, S. P. J. Whelan, A. M. van Oijen, S. C. Harrison,
873 Mechanism of membrane fusion induced by vesicular stomatitis virus G protein. *Proc National*
874 *Acad Sci*. 114, E28–E36 (2017).

875 35. B. Meng, A. Abdullahi, I. A. T. M. Ferreira, N. Goonawardane, A. Saito, I. Kimura, D.
876 Yamasoba, P. P. Gerber, S. Fatihi, S. Rathore, S. K. Zepeda, G. Papa, S. A. Kemp, T. Ikeda, M.
877 Toyoda, T. S. Tan, J. Kuramochi, S. Mitsunaga, T. Ueno, K. Shirakawa, A. Takaori-Kondo, T.
878 Brevini, D. L. Mallery, O. J. Charles, T. C.-N. B. C.-19 Collaboration, S. Baker, G. Dougan, C.
879 Hess, N. Kingston, P. J. Lehner, P. A. Lyons, N. J. Matheson, W. H. Ouwehand, C. Saunders,
880 C. Summers, J. E. D. Thaventhiran, M. Toshner, M. P. Weekes, P. Maxwell, A. Shaw, A. Bucke,
881 J. Calder, L. Canna, J. Domingo, A. Elmer, S. Fuller, J. Harris, S. Hewitt, J. Kennet, S. Jose, J.
882 Kourampa, A. Meadows, C. O'Brien, J. Price, C. Publico, R. Rastall, C. Ribeiro, J. Rowlands, V.
883 Ruffolo, H. Tordesillas, B. Bullman, B. J. Dunmore, S. Gräf, J. Hodgson, C. Huang, K. Hunter,
884 E. Jones, E. Legchenko, C. Matara, J. Martin, F. Mescia, C. O'Donnell, L. Pointon, J. Shih, R.
885 Sutcliffe, T. Tilly, C. Treacy, Z. Tong, J. Wood, M. Wylot, A. Betancourt, G. Bower, C. Cossetti,
886 A. D. Sa, M. Epping, S. Fawke, N. Gleadall, R. Grenfell, A. Hinch, S. Jackson, I. Jarvis, B.
887 Krishna, F. Nice, O. Omarjee, M. Perera, M. Potts, N. Richoz, V. Romashova, L. Stefanucci, M.
888 Strezlecki, L. Turner, E. M. D. D. D. Bie, K. Bunclark, M. Josipovic, M. Mackay, H. Butcher, D.
889 Caputo, M. Chandler, P. Chinnery, D. Clapham-Riley, E. Dewhurst, C. Fernandez, A. Furlong,
890 B. Graves, J. Gray, S. Hein, T. Ivers, E. L. Gresley, R. Linger, M. Kasanicki, R. King, S. Meloy,
891 A. Moulton, F. Muldoon, N. Ovington, S. Papadia, C. J. Penkett, I. Phelan, V. Ranganath, R.
892 Paraschiv, A. Sage, J. Sambrook, I. Scholtes, K. Schon, H. Stark, K. E. Stirrups, P. Townsend,
893 N. Walker, J. Webster, T. G. to P. J. (G2P-J. Consortium, E. P. Butlertanaka, Y. L. Tanaka, J.
894 Ito, K. Uriu, Y. Kosugi, M. Suganami, A. Oide, M. Yokoyama, M. Chiba, C. Motozono, H.
895 Nasser, R. Shimizu, K. Kitazato, H. Hasebe, T. Irie, S. Nakagawa, J. Wu, M. Takahashi, T.
896 Fukuhara, K. Shimizu, K. Tsushima, H. Kubo, Y. Kazuma, R. Nomura, Y. Horisawa, K. Nagata,
897 Y. Kawai, Y. Yanagida, Y. Tashiro, K. Tokunaga, S. Ozono, R. Kawabata, N. Morizako, K.
898 Sadamasu, H. Asakura, M. Nagashima, K. Yoshimura, E.-C. Consortium, P. Cárdenas, E.
899 Muñoz, V. Barragan, S. Márquez, B. Prado-Vivar, M. Becerra-Wong, M. Caravajal, G. Trueba,
900 P. Rojas-Silva, M. Grunauer, B. Gutierrez, J. J. Guadalupe, J. C. Fernández-Cadena, D.
901 Andrade-Molina, M. Baldeon, A. Pinos, J. E. Bowen, A. Joshi, A. C. Walls, L. Jackson, D.
902 Martin, K. G. C. Smith, J. Bradley, J. A. G. Briggs, J. Choi, E. Madissoon, K. B. Meyer, P.
903 Mlcochova, L. Ceron-Gutierrez, R. Doffinger, S. A. Teichmann, A. J. Fisher, M. S. Pizzuto, A. de
904 Marco, D. Corti, M. Hosmillo, J. H. Lee, L. C. James, L. Thukral, D. Veesler, A. Sigal, F.
905 Sampaziotis, I. G. Goodfellow, K. Sato, R. K. Gupta, Altered TMPRSS2 usage by SARS-CoV-2
906 Omicron impacts infectivity and fusogenicity. *Nature*. 603, 706–714 (2022).

907 36. H. Zhao, L. Lu, Z. Peng, L.-L. Chen, X. Meng, C. Zhang, J. D. Ip, W.-M. Chan, A. W.-H.
908 Chu, K.-H. Chan, D.-Y. Jin, H. Chen, K.-Y. Yuen, K. K.-W. To, SARS-CoV-2 Omicron variant
909 shows less efficient replication and fusion activity when compared with Delta variant in
910 TMPRSS2-expressed cells. *Emerg Microbes Infec*. 11, 277–283 (2022).

911 37. D. Bojkova, M. Widera, S. Ciesek, M. N. Wass, M. Michaelis, J. Cinatl, Reduced interferon
912 antagonism but similar drug sensitivity in Omicron variant compared to Delta variant of SARS-
913 CoV-2 isolates. *Cell Res*. 32, 319–321 (2022).

914 38. R. M. Effros, F. P. Chinard, The in vivo pH of the extravascular space of the lung. *J Clin*
915 *Invest*. 48, 1983–1996 (1969).

916 39. R. D. de Vries, K. S. Schmitz, F. T. Bovier, C. Predella, J. Khao, D. Noack, B. L. Haagmans,
917 S. Herfst, K. N. Stearns, J. Drew-Bear, S. Biswas, B. Rockx, G. McGill, N. V. Dorrello, S. H.
918 Gellman, C. A. Alabi, R. L. de Swart, A. Moscona, M. Porotto, Intranasal fusion inhibitory
919 lipopeptide prevents direct-contact SARS-CoV-2 transmission in ferrets. *Sci New York N Y*. 371,
920 1379–1382 (2021).

921 40. F. Aguet, S. Upadhyayula, R. Gaudin, Y. Chou, E. Cocucci, K. He, B.-C. Chen, K.
922 Mosaliganti, M. Pasham, W. Skillern, W. R. Legant, T.-L. Liu, G. Findlay, E. Marino, G. Danuser,
923 S. Megason, E. Betzig, T. Kirchhausen, Membrane dynamics of dividing cells imaged by lattice
924 light-sheet microscopy. *Mol Biol Cell*. 27, 3418–3435 (2016).

925 41. A. H. Abdelhakim, E. N. Salgado, X. Fu, M. Pasham, D. Nicastro, T. Kirchhausen, S. C.
926 Harrison, Structural Correlates of Rotavirus Cell Entry. *Plos Pathog*. 10, e1004355 (2014).

927 42. E. Cocucci, F. Aguet, S. Boulant, T. Kirchhausen, The First Five Seconds in the Life of a
928 Clathrin-Coated Pit. *Cell*. 150, 495–507 (2012).

929 43. Y.-Y. Chou, S. Upadhyayula, J. Houser, K. He, W. Skillern, G. Scanavachi, S. Dang, A.
930 Sanyal, K. G. Ohashi, G. D. Caprio, A. J. B. Kreutzberger, T. J. Vadakkan, T. Kirchhausen,
931 Inherited nuclear pore substructures template post-mitotic pore assembly. *Dev Cell*. 56, 1786-
932 1803.e9 (2021).

933 44. Y. Chen, N. C. Deffenbaugh, C. T. Anderson, W. O. Hancock, Molecular counting by
934 photobleaching in protein complexes with many subunits: best practices and application to the
935 cellulose synthesis complex. *Mol Biol Cell*. 25, 3630–3642 (2014).

936

ACKNOWLEDGMENTS:

We thank Stephen C Harrison for comments, suggestions, and extensive editorial assistance and members of our laboratories for help and encouragement; the staff at HUSLAB Virology and Immunology for providing human nasal swabs for virus isolation, to Suvi Kuivanen and Teemu Smura for virus propagation, sequencing and discussions, and Sanna Mäki for excellent technical work; Elliott Somerville (Kirchhausen laboratory) for excellent laboratory management; Tegy John Vadakkan for maintaining the spinning disc confocal microscope; Lena Tveriakhina (Blacklow laboratory, Harvard Medical School) for western blot analysis.

Funding:

NIH Maximizing Investigators' Research Award (MIRA) GM130386 (TK)
NIH Grant AI163019 (SPJW, TK)
Danish Technical University (TK)
SANA (TK)
Harvard Virology Program, NIH training Grant T32 AI07245 postdoctoral fellowship (AJBK)
Academy of Finland research grant 318434 (GB, RO)
Academy of Finland research grants 335527 and 336490 (OV)
Helsinki University Hospital Funds TYH2018322 (OV)
University of Helsinki Graduate Program in Microbiology and Biotechnology (RO)

Author contributions:

Alex J.B. Kreutzberger carried all the experiments except those with human SARS-CoV-2 isolates. Louis-Marie Bloyet and Spencer Stumpf generated, characterized, and sequenced the recombinant virus VSV-eGFP-P-SARS-CoV-2 Whuhan. Zhuoming Liu generated, characterized, and sequenced the recombinant viruses VSV-eGFP-SARS-CoV-2 Delta and Omicron. Anwesha Sanyal generated SVGA-A ACE2 and SVGA-A ACE2 TMPRSS2, maintained the cells lines and assisted with infectivity assays. Catherine A. Doyle helped analyzed data and carried out some VSV-SARS-CoV-2 infection assays. Elliott Somerville helped with virus sample preparation for DNA sequence. Gustavo Scanavachi and Anand Saminathan helped collect LLSM imaging data. Giuseppe Di Caprio set up the single particle data analysis pipeline. Volker Kiessling developed the LabVIEW-based viewer, simulated data and produced the single-particle MSD fitting algorithm. Sean P. J. Whelan oversaw the work to generate and characterize the VSV-chimeras, participated in early discussions, and helped edit portions of the manuscript. Giuseppe Balistreri guided the work on SARS-CoV-2 and performed infection assays, imaging, and image analysis.

971 Ravi Ojha performed SARS-CoV-2 infection assays, imaging, and image analysis. Olli Vapalahti
972 coordinated the BSL3 work, provided SARS-CoV-2 and performed virus sequencing.
973 Tom Kirchhausen and Alex J.B. Kreutzberger were responsible for the overall design of the study;
974 Tom Kirchhausen drafted the manuscript with direct input from Alex J.B. Kreutzberger; all authors
975 commented on the manuscript.
976
977 **Competing interests**
978 T.K. is a member of the Medical Advisory Board of AI Therapeutics, Inc. The other authors declare
979 no competing interests.
980
981 **Data and material availability**
982 All materials and data generated in this study are available upon request. Further information and
983 requests for resources and reagents should be directed to and will be fulfilled by the lead contact,
984 Dr. Tom Kirchhausen, mailto:kirchhausen@crystal.harvard.edu. Requests for VSV-SARS-CoV-2
985 chimeras and their materials transfer agreements (MTA) should be directed to and will be fulfilled
986 by Dr. Sean Whelan, spjwhelan@wustl.edu. This study did not generate any unique large-scale
987 datasets. The LabView code for visualizing trajectories is available for download (GITHUB).

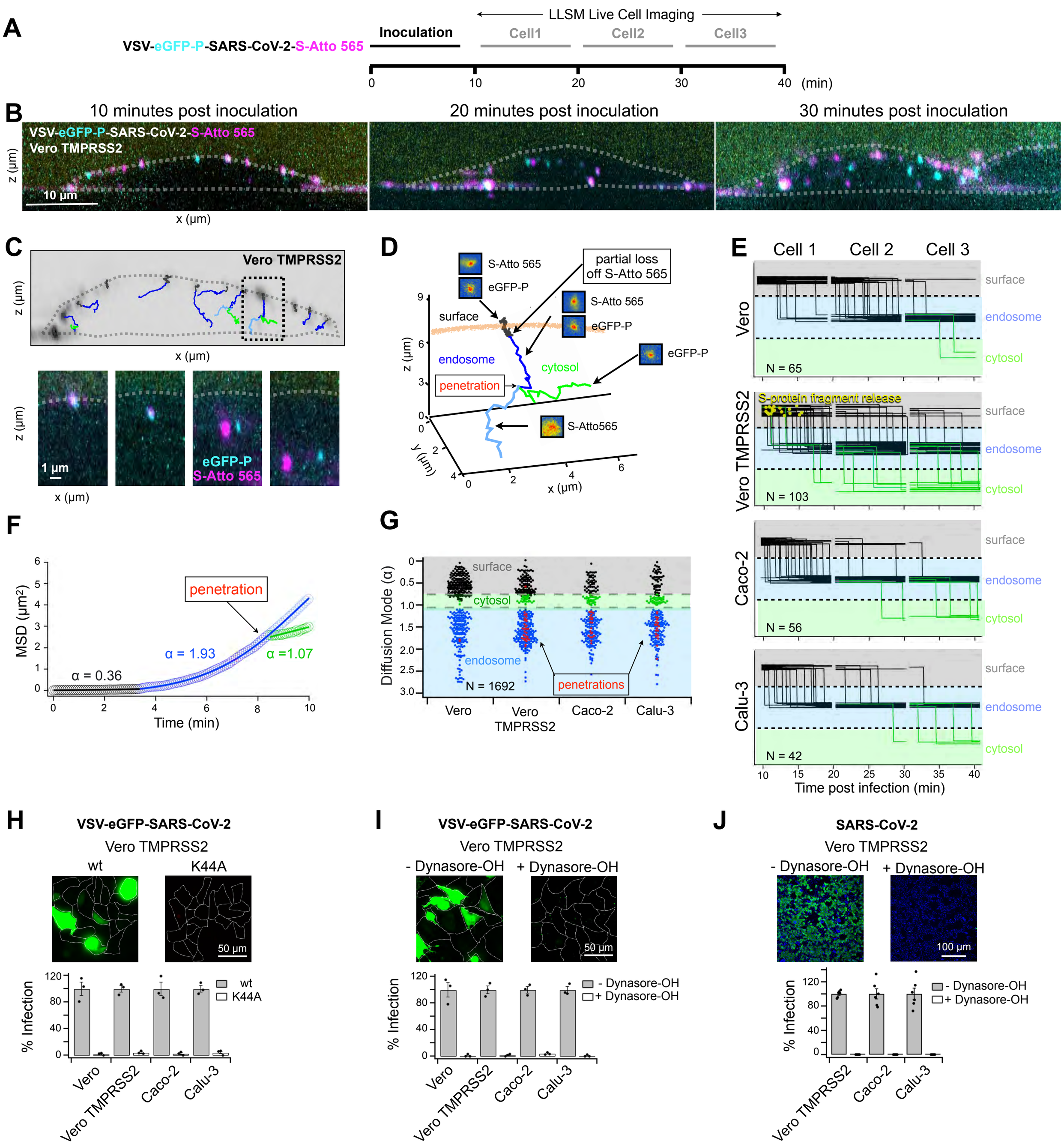
A
VSV-eGFP-P-SARS-CoV-2-S-Atto 565
Inoculation
LLSM Live Cell Imaging
Cell1
Cell2
Cell3
0
10
20
30
40
(min)
B
10 minutes post inoculation
20 minutes post inoculation
30 minutes post inoculation
VSV-eGFP-P-SARS-CoV-2-S-Atto 565
Vero TMPRSS2
z (µm)
10 µm
x (µm)
C
Vero TMPRSS2
z (µm)
x (µm)
1 µm
eGFP-P
S-Atto 565
D
S-Atto 565
eGFP-P
partial loss
off S-Atto 565
surface
endosome
cytosol
penetration
S-Atto565
z (µm)
y (µm)
x (µm)
E
Cell 1
Cell 2
Cell 3
Vero
Vero TMPRSS2
Caco-2
Calu-3
surface
endosome
cytosol
S-protein fragment release
N = 65
N = 103
N = 56
N = 42
Time post infection (min)
F
MSD (µm²)
penetration
α = 0.36
α = 1.93
α =1.07
Time (min)
G
Diffusion Mode (α)
surface
cytosol
endosome
N = 1692
penetrations
Vero
Vero TMPRSS2
Caco-2
Calu-3
H
VSV-eGFP-SARS-CoV-2
Vero TMPRSS2
wt
K44A
50 µm
% Infection
wt
K44A
Vero
Vero TMPRSS2
Caco-2
Calu-3
I
VSV-eGFP-SARS-CoV-2
Vero TMPRSS2
- Dynasore-OH
+ Dynasore-OH
50 µm
% Infection
- Dynasore-OH
+ Dynasore-OH
Vero
Vero TMPRSS2
Caco-2
Calu-3
J
SARS-CoV-2
Vero TMPRSS2
- Dynasore-OH
+ Dynasore-OH
100 µm
% Infection
- Dynasore-OH
+ Dynasore-OH
Vero TMPRSS2
Caco-2
Calu-3

Figure 1

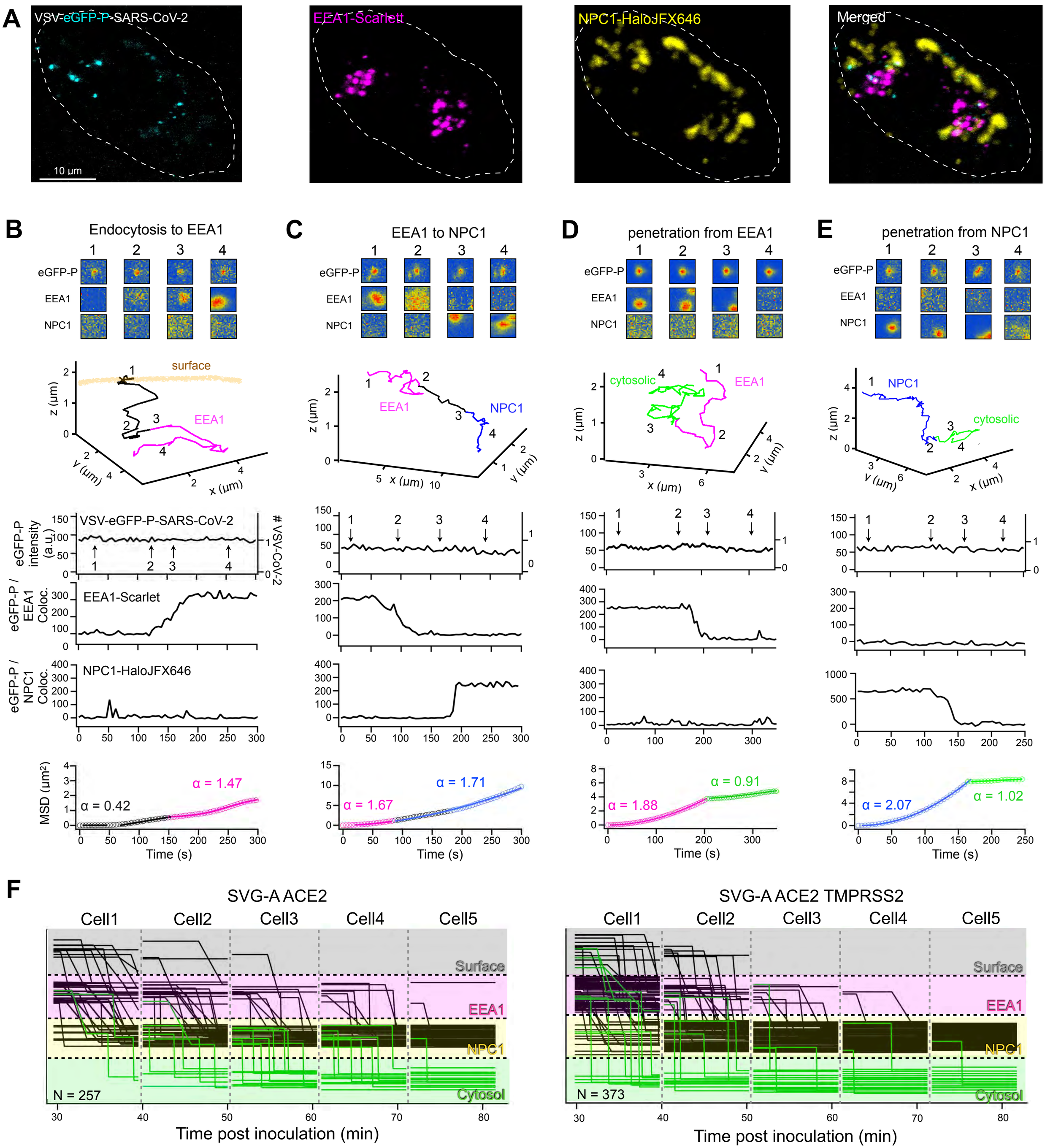
A
VSV-eGFP-P-SARS-CoV-2
10 µm
EEA1-Scarlett
NPC1-HaloJFX646
Merged
B
Endocytosis to EEA1
C
EEA1 to NPC1
D
penetration from EEA1
E
penetration from NPC1
eGFP-P
EEA1
NPC1
surface
cytosolic
z (µm)
x (µm)
y (µm)
VSV-eGFP-P-SARS-CoV-2
VSV-CoV-2
eGFP-P intensity (a.u.)
EEA1-Scarlet
eGFP-P / EEA1 Coloc.
NPC1-HaloJFX646
eGFP-P / NPC1 Coloc.
MSD (µm²)
Time (s)
α = 0.42
α = 1.47
α = 1.67
α = 1.71
α = 1.88
α = 0.91
α = 2.07
α = 1.02
F
SVG-A ACE2
SVG-A ACE2 TMPRSS2
Cell1
Cell2
Cell3
Cell4
Cell5
Surface
EEA1
NPC1
Cytosol
N = 257
N = 373
Time post inoculation (min)

Figure 2

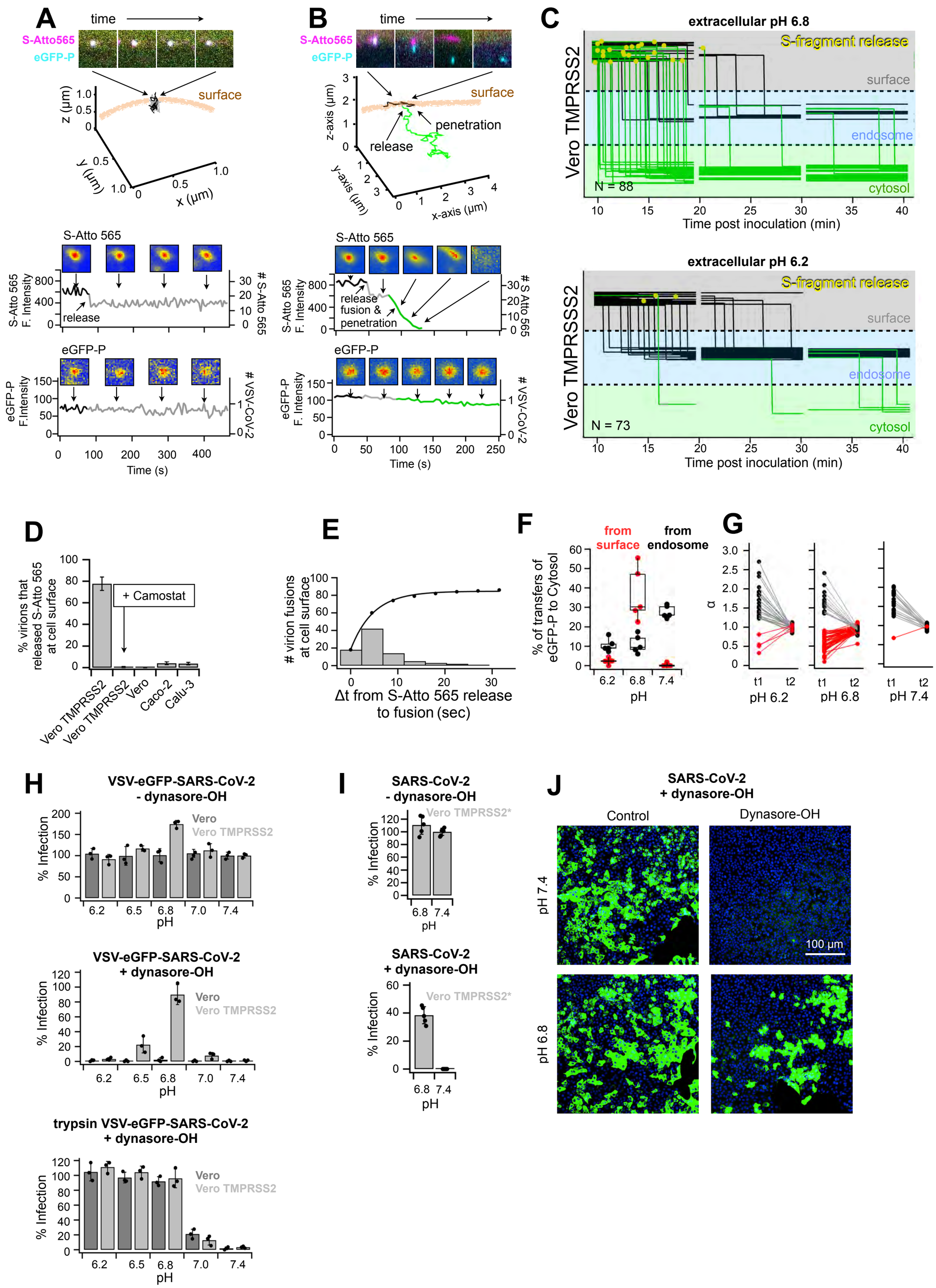
A
time
S-Atto565
eGFP-P
surface
z (µm)
y (µm)
x (µm)
S-Atto 565
S-Atto 565 F. Intensity
S-Atto 565
release
eGFP-P
eGFP-P F.Intensity
VSV-CoV-2
Time (s)
B
time
S-Atto565
eGFP-P
surface
penetration
release
z-axis (µm)
y-axis (µm)
x-axis (µm)
S-Atto 565
S-Atto 565 F. Intensity
S-Atto 565
release
fusion &
penetration
eGFP-P
eGFP-P F. Intensity
VSV-CoV-2
Time (s)
C
extracellular pH 6.8
Vero TMPRSS2
S-fragment release
surface
endosome
cytosol
N = 88
Time post inoculation (min)
extracellular pH 6.2
Vero TMPRSSS2
S-fragment release
surface
endosome
cytosol
N = 73
Time post inoculation (min)
D
% virions that released S-Atto 565 at cell surface
+ Camostat
Vero TMPRSS2
Vero TMPRSS2
Vero
Caco-2
Calu-3
E
virion fusions at cell surface
Δt from S-Atto 565 release to fusion (sec)
F
from surface
from endosome
% of transfers of eGFP-P to Cytosol
pH
G
α
t1
t2
pH 6.2
pH 6.8
pH 7.4
H
VSV-eGFP-SARS-CoV-2 - dynasore-OH
% Infection
Vero
Vero TMPRSS2
pH
VSV-eGFP-SARS-CoV-2 + dynasore-OH
trypsin VSV-eGFP-SARS-CoV-2 + dynasore-OH
I
SARS-CoV-2 - dynasore-OH
Vero TMPRSS2*
% Infection
pH
SARS-CoV-2 + dynasore-OH
J
SARS-CoV-2 + dynasore-OH
Control
Dynasore-OH
pH 7.4
pH 6.8
100 µm

Figure 3

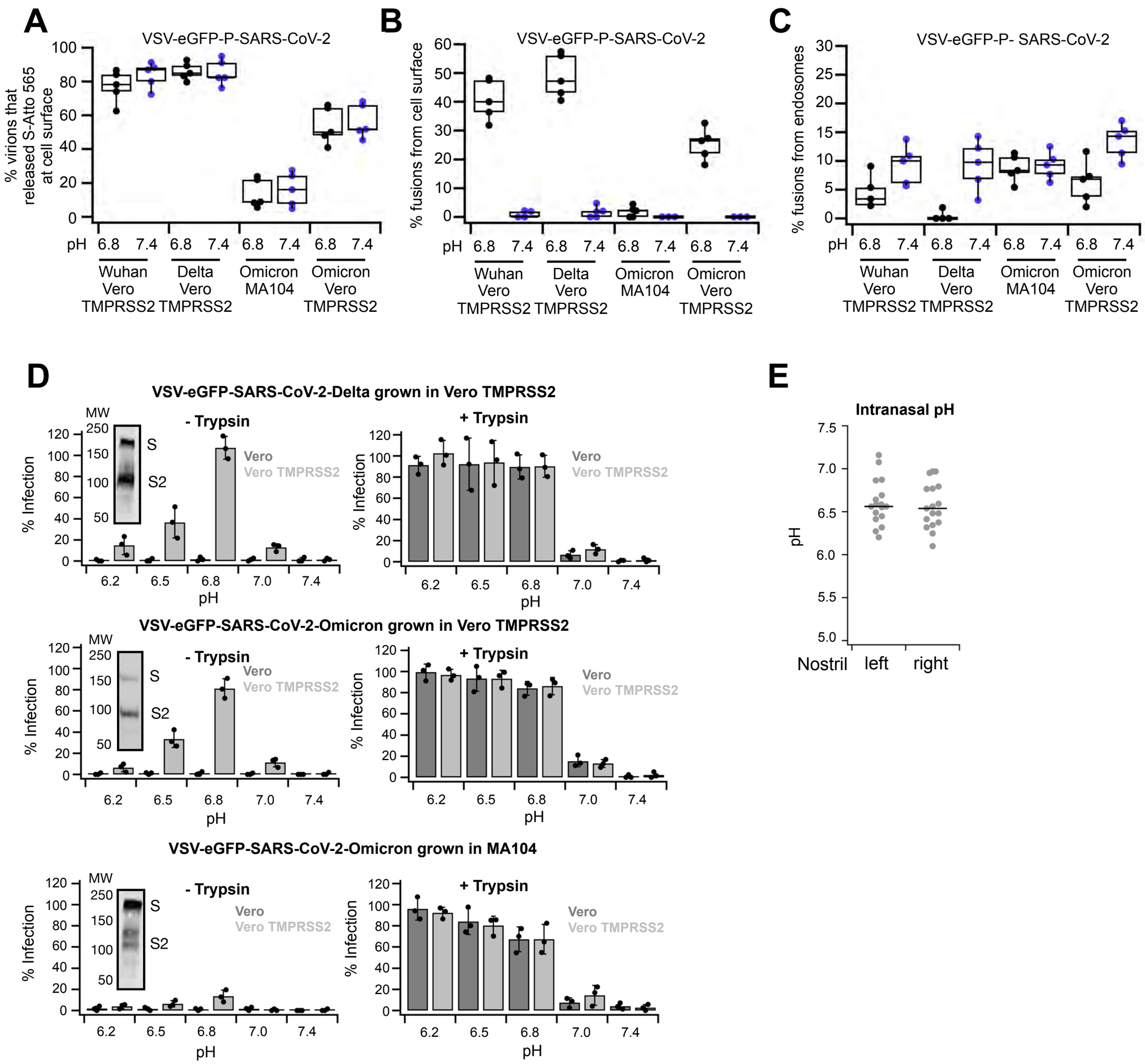
A
VSV-eGFP-P-SARS-CoV-2
% virions that released S-Atto 565 at cell surface
pH 6.8 7.4 6.8 7.4 6.8 7.4 6.8 7.4
Wuhan Vero TMPRSS2
Delta Vero TMPRSS2
Omicron MA104
Omicron Vero TMPRSS2
B
VSV-eGFP-P-SARS-CoV-2
% fusions from cell surface
C
VSV-eGFP-P- SARS-CoV-2
% fusions from endosomes
D
VSV-eGFP-SARS-CoV-2-Delta grown in Vero TMPRSS2
VSV-eGFP-SARS-CoV-2-Omicron grown in Vero TMPRSS2
VSV-eGFP-SARS-CoV-2-Omicron grown in MA104
MW
S
S2
- Trypsin
+ Trypsin
Vero
Vero TMPRSS2
% Infection
pH
E
Intranasal pH
Nostril left right

Figure 4

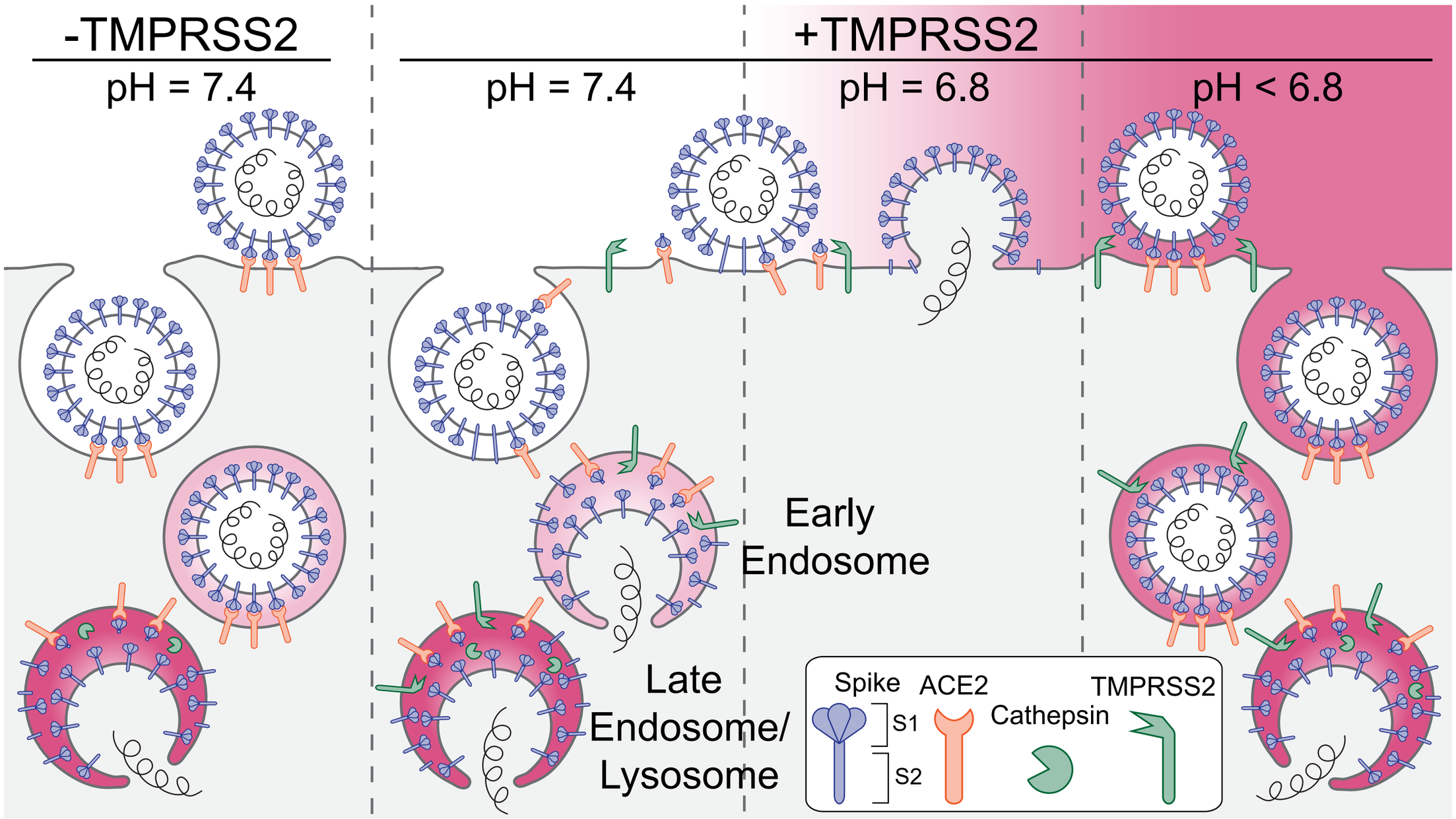
-TMPRSS2
pH = 7.4
+TMPRSS2
pH = 7.4
pH = 6.8
pH < 6.8
Early
Endosome
Late
Endosome/
Lysosome
Spike
ACE2
TMPRSS2
S1
S2
Cathepsin

Figure 5